Applied Energy 353 (2024) 122004

Contents lists available at ScienceDirect

Applied Energy

journal homepage: www.elsevier.com/locate/apenergy

Predicting PEMFC performance from a volumetric image of catalyst layer structure using pore network modeling

Mohammad Amin Sadeghi [a], Zohaib Atiq Khan [a,b], Mehrez Agnaou [a], Leiming Hu [c,d], Shawn Litster [c], Anusorn Kongkanand [e], Elliot Padgett [f], David A. Muller [f], Tomislav Friscic [g], Jeff Gostick [a,*]

[a] Department of Chemical Engineering, University of Waterloo, ON, Canada
[b] Department of Chemical, Polymer and Composite Materials Engineering, University of Engineering and Technology Lahore, New Campus, Pakistan
[c] Department of Mechanical Engineering, Carnegie Mellon University, Pittsburgh, PA, USA
[d] Chemistry and Nanoscience Center, National Renewable Energy Lab, Golden, CO, USA
[e] Fuel Cell Business, General Motors, Pontiac, MI, USA
[f] School of Applied and Engineering Physics, Cornell University, Ithaca, NY, USA
[g] Department of Chemistry, University of Birmingham, UK

HIGHLIGHTS

- A 4-phase pore network model was extracted from a 3D image with 4 nm resolution.
- Experimental polarization curves were well matched without fitting parameters.
- Degradation due to ECSA loss was matched by deleting Pt sites from the network.

GRAPHICAL ABSTRACT

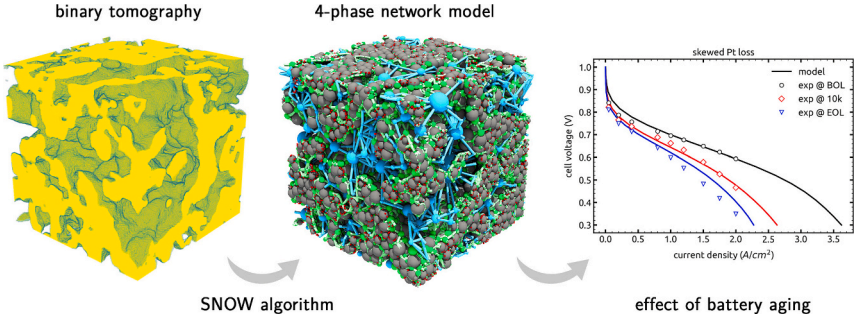

ARTICLE INFO

Keywords:
Hydrogen fuel cell
Catalyst layer
Pt degradation
Microscale simulation
Multiphysics
Pore network model

ABSTRACT

A pore-scale model of a PEMFC cathode catalyst layer was developed using the pore network approach and used to predict polarization behavior. A volumetric image of a PEMFC catalyst layer was obtained using FIB-SEM with 4 nm resolution in all 3 directions. The original image only differentiated between solid and void, so a simple but effective algorithm was developed to insert tightly packed, but non-overlapping carbon spheres into the solid phase, which were then decorated with catalyst sites. The resultant image was a 4-phase image containing void, ionomer, carbon, and catalyst, each in proportion to the known Pt loading, carbon-to-ionomer ratio, and porosity. A multiphase pore network model was extracted from this image, and multiphysics simulations were conducted to predict the polarization behavior of an operating cell. It was shown that not only can beginning of life polarization performance be predicted with minimal fitting parameters, but degraded performance 30 k cycles was also well captured with no additional fitting. This latter result was accomplished by deleting catalyst sites from the network in proportion to the experimentally observed distribution of electrochemical surface area

* Corresponding author.
E-mail address: jgostick@uwaterloo.ca (J. Gostick).

https://doi.org/10.1016/j.apenergy.2023.122004
Received 28 July 2023; Received in revised form 14 September 2023; Accepted 20 September 2023
Available online 4 October 2023

loss, obtained from TEM image of catalyst loading. The model included partitioning of oxygen into the ionomer phase, explicitly incorporating the oxygen transport resistance which dominates cell performance at higher current density. Although Knudsen diffusion is present at the scales present ($< 100\,nm$), it represented a negligible fraction of the total transport resistance, which was dominated by the low solubility and slow diffusivity in the ionomer phase. This work showed that the performance of a typical PEMFC is highly dependent on the structural details of the catalyst layer, to the extent that polarization curves can be well predicted by direct inspection of an image of the catalyst layer. This work paves the way for a deeper understanding of the structure-performance relationship in these complex materials and the search for optimized catalyst layer designs.

1. Introduction

To migrate toward a sustainable energy economy, the key is increasing the usage of renewable energy [1]. Hydrogen is one of the most practical renewable energy vectors for storage, transportation, as well as delivering significant amounts of energy at both small and large scales reaching well into the terawatt hour range [2]. Hydrogen fuel cells are electrochemical devices that can directly convert chemical energy stored in hydrogen into electricity. Unlike internal combustion engines, this direct conversion leads to a much higher energy conversion efficiency (theoretically ~83%) [3] in proton exchange membrane fuel cells (PEMFC), which makes them a promising alternative [4,5]. Although fuel cell cars are being commercially manufactured, they are still expensive partly due to the use of expensive noble catalysts such as platinum and therefore, they are not viable for most consumers. Furthermore, for use in heavy duty vehicles such as trucks, durability is another challenge that must be addressed [6]. This is especially important since for medium and heavy-duty vehicles, fuel cells are more desirable than Li-ion batteries because of two important factors: faster refueling times, and higher power density, which leads to a lighter overall weight [7].

To reduce the cost of fuel cells, one of the key components to consider is the catalyst layer (CL), which accounts for 26% to 41% of the total cost of a fuel cell system depending on how many units per year are manufactured [8]. In addition to being the most expensive component, the CL is where most of the degradation occurs. Therefore, improving the CL can significantly accelerate the commercialization of fuel cells. One avenue is by optimizing the CL microstructure to maximize the generated power density, but this is especially challenge to its complexity. The CL is a multiscale, multiphase porous material composed of a carbon backbone decorated with catalyst particles (usually platinum or alloy thereof) and coated with a film of ionomer (e.g., Nafion). This plays host to complex transport phenomena at pore scale which cannot be experimentally studied [9], especially that the CL is very thin (0.1–50 um) [10]. With these constraints, modeling and simulation can be used to study these pore-scale phenomena in a controlled fashion to provide fundamental insights for designing better CL microstructures. Furthermore, it can be used to develop high-fidelity digital twins of the entire PEMFC system to be used for diagnosis, performance predictions, and ultimately lifetime predictions [11,12].

Multiphysics modeling of the CL began with the pioneering work of Bernardi and Verbrugge [13], who presented a 1D homogeneous continuum model to study the system. Inspired by experimental imaging data, another category known as agglomerate models were introduced in which it is assumed that carbon particles form certain agglomerates. Due to their closer representation of experimental observations [14,15], they gained popularity and are still in common use [14–27]. To construct an agglomerate model, the structure of the agglomerate is approximated via a set of parameters such as porosity, radius, etc. Then, transport equations are solved for a single agglomerate and the average rates are used in a large-scale homogeneous continuum model that spans the entire CL thickness. Because agglomerate models are essentially phenomenological, their predictive capability beyond the assumed structure is limited. Furthermore, they require knowledge of pore-scale parameters either through direct measurement, which is not trivial for ultra thin materials such as the CL, or through closure relations from pore-scale models, in which the pore-scale geometry is explicitly considered. To design next generation CL electrodes, a pore-scale model which can directly capture the interplay between CL microstructure and performance is needed. One of the main challenges, which will be tackled in this work, is that conventional pore-scale models become computationally intractable when applied to the entire CL thickness.

In the early studies on pore-scale modeling of the CL, due to limited computing resources, the structure of the CL was approximated using idealized shapes such as regular lattice of spheres. Also, its multiphase nature had to be simplified, for instance by excluding discrete catalyst sites [28,29]. During the past two decades, as more computing resources have becoming available, more sophisticated realizations of the CL microstructure have been considered. These realizations come from two main sources: statistical reconstruction [30–33] (and more recently deep learning generative models [34]), which has been the dominant source, and three-dimensional imaging techniques such as X-ray computed tomography and focused ion beam SEM serial sectioning, both of which are becoming more common. The problem of computational tractability is exacerbated by the fact that the CL is a multiscale, multiphase, and multiphysics system. To make the problem numerically feasible, some studies have limited the scope to a single carbon agglomerate [35–38], while in others the coupled multiphysics transport has been neglected and instead the focus has been on exploring how pore-scale parameters such as Pt loading affect macroscopic properties such as effective diffusivity, etc. [39–42]. Very few studies, to the best of our knowledge, have performed pore-scale simulation of the entire CL thickness, but at the expense of hundreds or even thousands of CPU-hours per a single specified cell voltage/current density [43–45]. The massive computational requirements of these models significantly restrict their applicability as a tool for design optimization purposes. Furthermore, even in these studies, there has been some simplifications that might render the results less reliable. For instance, Chen et al. have entirely excluded proton transport in the CL based on the assumption that the voltage loss is negligible [44], which is questionable at high overpotentials.

In this work, we employ pore network modeling, which a substantially faster alternative to direct numerical simulations (DNS) of the CL, yet is able to maintain reasonable accuracy. Pore network models (PNM) have been widely used to study transport processes in fuel cell components, with an emphasis on predicting multiphase transport properties for use as closures in continuum models. Only a limited number of PNM studies have incorporated the electrochemical reaction to simulate cell performance, and even fewer have applied PNM to the catalyst layer [46,47]. The work of Wu et al. [46] is the most thorough model available in the literature, but it is based on a basic cubic lattice topology with simplistic assumptions about the geometrical properties of the pores and throats. They also assumed the ionomer phase was a thin coating on the inside of the void elements, rather than a network in its own right. In short, this early model was ground-breaking but limited by lack of real structural information on which to base their network. The model presented in the present work bridges this gap by extracting a multiscale, multiphase pore network from an experimentally obtained volumetric image of a catalyst layer, enable the model to explicitly account for all 4 phases present in the CL, namely void, ionomer, carbon, and platinum

(Pt). With regards to the length scales of the model, it covers from ∼4 nm, which is a single Pt nanoparticle, up to an almost 2 orders of magnitude larger ∼100 nm, which is the intra-agglomerate void space. With respect to the computational performance, we show that the proposed model provides at least 1000× speedup over to the state-of-the-art DNS pore-scale models when normalized for domain size considered. As for predictability, we show that the model is not only capable of matching experimental polarization data, but also it can predict the performance loss as a result of degradation to a reasonable accuracy, something that has previously not been done to the best of our knowledge.

2. Experimental

2.1. Catalyst layer production and testing

The CL samples studied here were prepared and used by Braaten et al. [48]. Specifically, Pt/Vu was used as the cathode catalyst and applied to the ionomer film from an ink slurry via a Meyer bar technique with an ionomer to carbon ratio of 0.8 and a Pt loading of 0.1 mg/cm^2. The experimental performance data reported here were taken from the stated paper, according to the testing procedures reported therein. The degradation data for the electrodes resulting from an accelerated stress testing protocol involving potential cycling was also taken from Braaten et al. [48].

2.2. Image acquisition and processing

The CL samples produced by Braaten et al. [48] were subsequently imaged using serial sectioning with focused ion-beam milling combined with scanning electron microscopy (FIB-SEM). Images were acquired using Helios PFIB UXe DualBeam G4 instrument. A total volume of $3 \times 3 \times 6.4$ μm was characterized, with an electron imaging pixel size of 2×2 nm, and a layer spacing of 4 nm. The FIB milling was conducted at 30 kV with a milling current of 0.23 nA. The electron imaging was operated at 10 kV and 1.4 nA. Image pre-processing included slice to slice alignment and homogenization the contrast/brightness of the overall image stack. The image segmentation was conducted using a customized MATLAB script. The segmented image stack was binned in the X and Y directions yielding a final voxel size of $4 \times 4 \times 4$ nm.

As was mentioned above, the fuel cell catalyst layer consists of 4 phases, namely void, ionomer, carbon, and Pt. However, only the void and solid phases are distinguishable in the obtained images. The solid phase itself consists of carbon, ionomer, and platinum, but are indistinguishable in the original images. To construct the simulation domain, an algorithm was developed that mimics the physical process of packing spheres into the given solid phase. This algorithm is outlined schematically in Fig. 1 and is further explained in the following subsections. 2D illustrations are used for clarity but the described algorithm was applied to the 3D images. For tuning the reconstruction algorithm, macroscopic metrics, namely, the void fraction, and I/C and Pt/C ratios, were used, which are available from experiment [48].

2.2.1. Addition of carbon particles

To reconstruct the carbon phase, we used a modified random sequential addition (RSA) algorithm, which we dub as *pseudo electrostatic packing*, to add tightly packed and physically connected carbon spheres to the solid phase. The steps are illustrated in Fig. 2. It starts by computing the distance transform of the foreground (solid phase indicated by yellow in Fig. 2(a)) as shown in Fig. 2(b), then proceeds by adding a sphere at the next largest available location. Fig. 2(c) shows the result adding 20 spheres. The key to the algorithm is that when a sphere is added, the region of the distance transform within a 2R band of the center point is set to zero as shown in Fig. 2(d). This effectively prevents any new spheres from being added which may overlap existing spheres since any peaks in the distance transform will be at least voxels away from an existing sphere. Subsequent spheres are added in a similar way, though the peaks in the distance transform tend to lie on the edge of the band of 0's around existing spheres. This leads to a clustering or agglomeration of particles as can be seen in Fig. 2(e). Note that the size of the band can be adjusted by using a value of $2R + c$ where c can be positive to create clearance or negative to give some overlap between particles. In this work some overlap was used to ensure particles were in good contact for subsequent image analysis. It is also possible for the spheres to protrude into the void phase by first dilating the foreground (i.e., Fig. 2(a)) by a few voxels, then proceeding as described above. This creates additional sites for insertion which will result in some spheres protruding beyond the solid phase as shown in Fig. 2(f), simulating imperfect ionomer coverage.

2.2.2. Addition of platinum nanoparticles

Once the "solid" phase was filled with the desired volume fraction of carbon particles, Pt nanoparticles were next applied onto the surface of the carbon. Each Pt nanoparticle is about 5 nm in diameter, which is roughly the resolution of the tomography image (4 nm) used here. Therefore, each Pt nanoparticle was assumed to fully occupy a single voxel in the tomography image. For reconstructing the Pt phase, the first step was to identify potential locations by finding the carbon particle boundaries. Some of these locations were then randomly chosen and those voxels were labeled as Pt. During this process some of the Pt nanoparticles are isolated within agglomerates and therefore contribute very little to the performance of the fuel cell, which is expected to also occur in a real catalyst layer. One limitation of the present approach is that Pt is not added to regions between two overlapping carbon particles since these regions are not identified as boundaries. This could be remedied by adding Pt prior to inserting the carbon spheres, for instance, but this complication was not necessary, since this only affected a small proportion of the total area. Finally, once the Pt/C backbone was constructed, the remaining "solid" phase was labeled as ionomer, which concludes the image preparation. Fig. 3 shows the procedure of obtaining a four-phase network model from this four-phase segmented image. As will be discussed later, the intermediate steps of

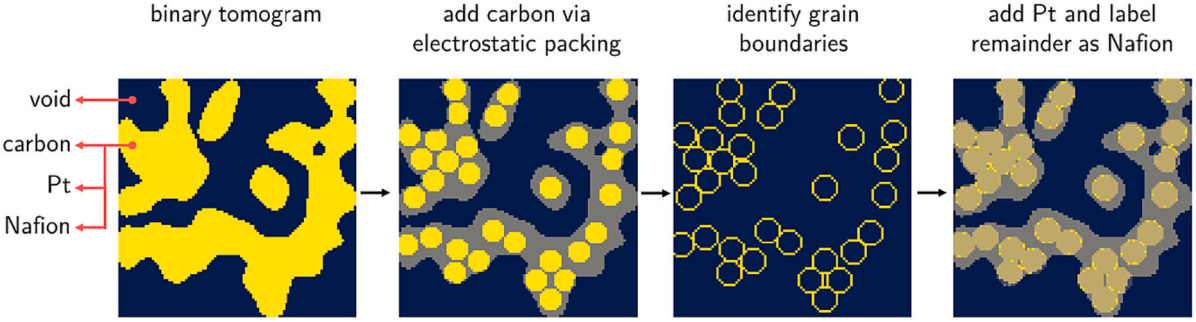

Fig. 1. Deconstruction of the "solid" phase in the binary tomogram into constituent phases: carbon, ionomer, and Pt.

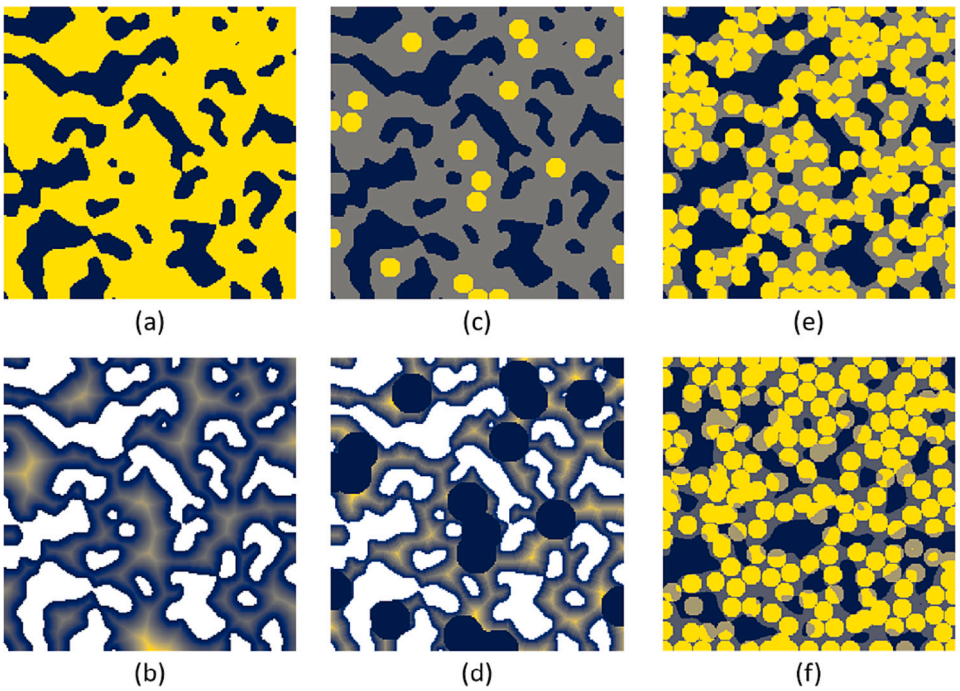

Fig. 2. Steps involved in the pseudo-electrostatic packing algorithm. (a) The original solid phase, (b) the distance transform of the solid phase with intensity values representing distance to nearest background pixel, (c) location of first 20 spheres, (d) the distance transform after 20 sphere additions showing the zeroed regions, (e) the result after many sphere insertions, (f) the result when some protrusion of the spheres into the void space was permitted.

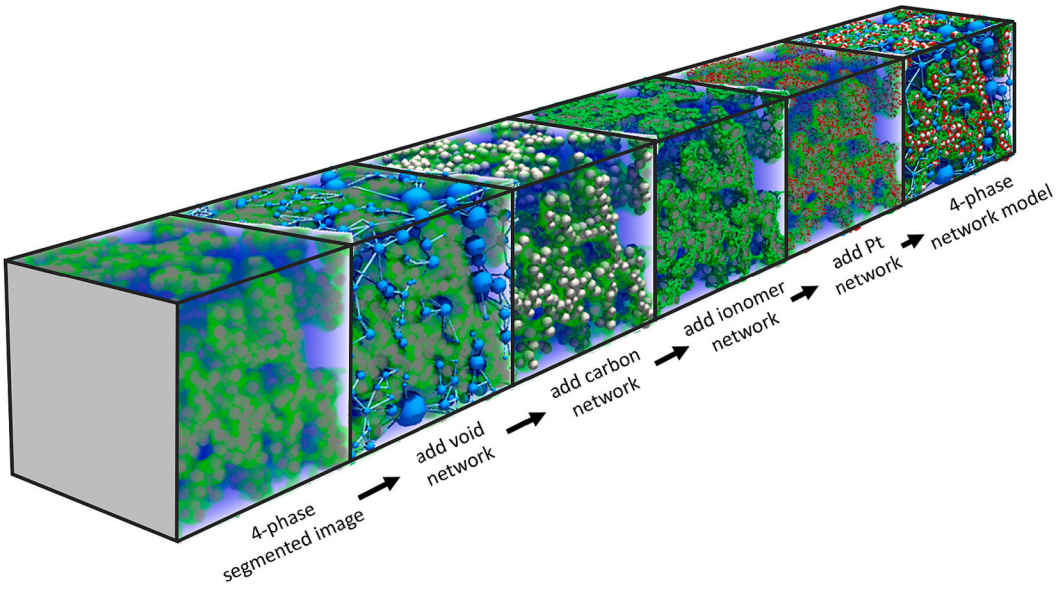

Fig. 3. An illustrative procedure of obtaining a 4-phase network model from a 4-phase segmented image. For clarity, only a small cubic cross-section of the image is shown.

obtaining individual network models for each phase as shown in this figure are shown as separate steps for clarity and are performed simultaneously in a single step in the SNOW algorithm.

2.2.3. *Network extraction*

Once the carbon and platinum particles were added, the result is a voxel image consisting of four distinct phases: carbon, platinum, ionomer (i.e., Nafion), and void. Fig. 4 shows a sample 2D cross-section of this four-phase voxel image colored based on the constituent phases. Using this voxel image, one could perform DNS directly on the image. However, performing DNS involves solving for many unknowns, which is practically impossible in a reasonable time for any substantially large section of the CL (i.e., the total thickness). Pore network modeling (PNM) is a pore-scale approach with a low computational cost in which the fine computational grid of the voxel image is essentially coarsened (via a network extraction algorithm) to produce a network of pores (nodes), with each pore representing a region in the voxel image. There are many network extraction algorithms in the literature, most of which are only capable of operating on binary images. We used the SNOW algorithm, which can operate on multiphase voxel images [49]. In addition, the SNOW algorithm is parallelized, which was helpful when applying to the large image used in this study [50]. Regarding the

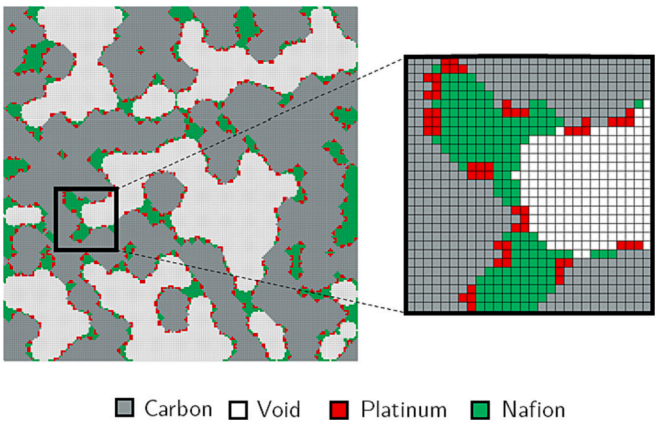

Fig. 4. Voxel image consisting of four distinct phases: carbon, platinum, ionomer, and void.

accuracy of the PNM approach, we did not perform separate validation simulations to compare macroscopic metrics such as effective diffusivity since performing DNS on the entire tomogram was not computationally feasible for reasons mentioned. Instead, we validated the PNM approach by reproducing the experimental polarization curve measured from the actual electrode.

Fig. 5 shows the process of generating the final four-phase pore network model. Beginning with the four-phase voxel image, using the SNOW algorithm, the carbon, void, ionomer, and Pt phases are segmented separately, and then the segmented image is converted into a single multiphase pore network model in one step. Common network extraction methods such as the maximal ball algorithm [51] only operate on binary images and therefore, operating on multiphase tomograms is one of the key advantages of the SNOW algorithm. The reader can refer to the work of Khan et al. [49] for the details of how the segmented image is converted into a multiphase network model. Note that in this figure, the "network extraction" step is shown for illustration purposes only and is not an actual step. The SNOW algorithm directly converts the segmented image into a multiphase network model. As for the software, we used PoreSpy [52] for network extraction, and OpenPNM [53] for transport simulations, both of which are open-source, written in Python, and publicly accessible.

2.2.4. Validating reconstructed image and extracted network

Inserting carbon spheres and adding platinum sites, as described in the above sections, was conducted to ensure the structural properties of the image matched the experimental values for the material. To start with, the segmented binary image had a porosity of 0.45, which corresponds well with the value of 0.48 obtained from a mass balance based on the sample composition, using the nominal platinum loading of 0.1 mg/cm^2 [48] and assuming the density of the ionomer was 1.8 g/cm^3 [54].

Carbon spheres were inserted using the described pseudo-electrostatic algorithm until no further spheres could be accommodated within the solid phase. The spheres were allowed to overlap each other by 1 voxel and allowed to protrude into the void space by 1 voxel. This produced an ionomer to carbon volume ratio of 1.004. After accounting for the density of ionomer and carbon, the weight ratio was 0.801, matching the value of 0.8 used in the experiment [48]. All carbon spheres were set to 10 voxels in diameter, which equates with 40 *nm* at the image resolution used here. Using a uniform particle size was necessary for computational performance of the sphere insertion algorithm. This simplification was deemed acceptable since transport of ions and dissolved oxygen in the ionomer phase was of stronger interest than electron conduction (In fact, electron conduction was ultimately neglected in the simulations to save time since negligible voltage drop was observed). Transport in the ionomer phase is controlled by the volume fraction of ionomer and the tortuosity. The volume fraction of ionomer was correct, and the tortuosity is dictated by both macroscopic distribution of the solid, which was obtained from the experimental

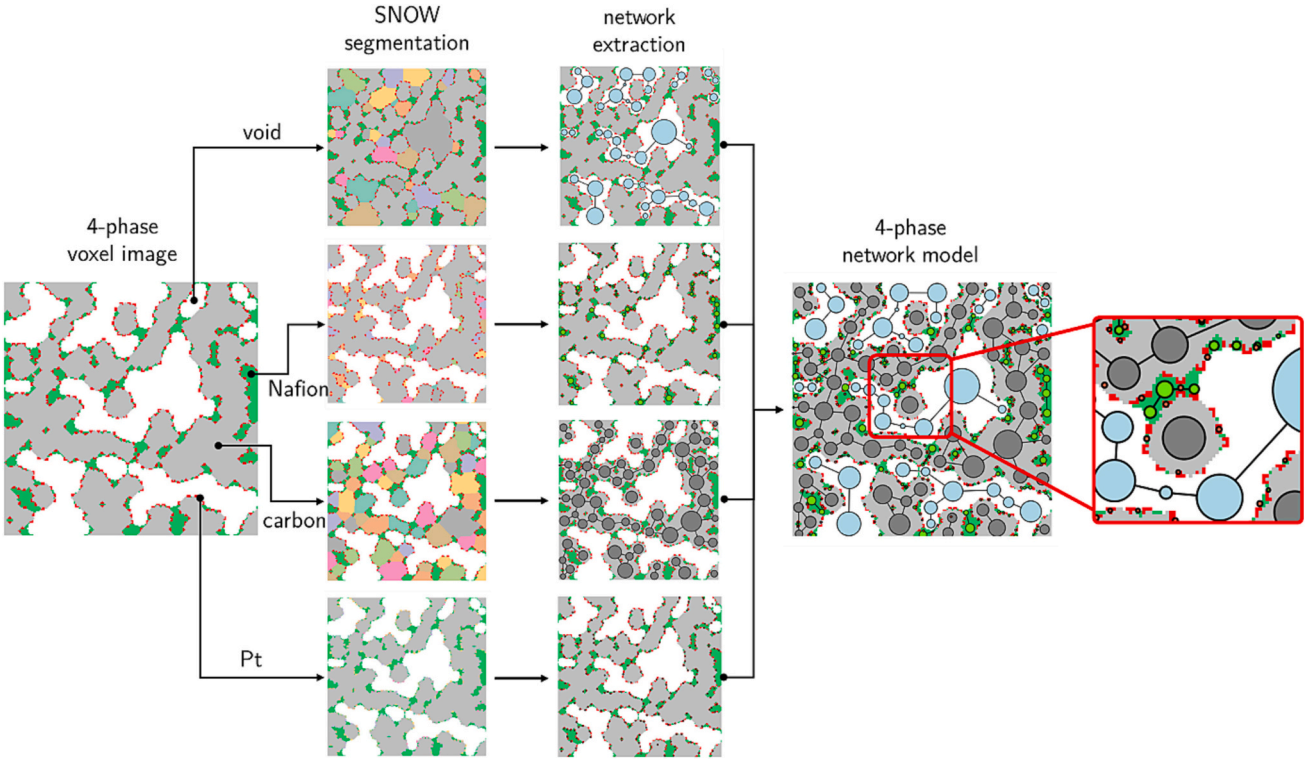

Fig. 5. The process of building a 4-phase network model from the segmented CL X-ray tomogram. For visual clarity, interconnections between phases are not shown (ex. void-ionomer, etc.).

image, and by the microscopic distribution of spheres. The use of tightly packed, uniform sized particles provided a good first approximation for this additional tortuosity at the microscale level. Although applying a carbon particle size distribution might alter this microscale tortuosity further, but it is safe to assume that this would not substantially alter the overall transport behavior in the ionomer given the weight of the mentioned factors.

Lastly, platinum nanoparticles were added to the perimeter of the spheres to match the experimental platinum loading of $\sim 0.1\ mg_{Pt}/cm^2$. Because of the method used it was not possible to add platinum to the regions where spheres overlapped. Missing these sites does not impact the simulation since they were not electrochemically active; however, to avoid overloading the exposed portions of the catalyst the number of platinum sites added was reduced by 10%. By counting the number of platinum sites and assuming each site was $4\ nm$ cube with 5 sides exposed, the total surface area in the image was $53\ m^2/g_{Pt}$ (adjusted for 10% reduction in loading). This is somewhat lower than the $\sim 82\ m^2/g_{Pt}$ measured experimentally considering that real Pt particles have surface roughness which was not accounted for here, this discrepancy is considered acceptable. Moreover, this can be compensated for by the exchange current density which was used an adjustable parameter in the present model. Ultimately for the present work, the more important feature is that the spatial distribution of Pt sites throughout the domain was close to the real system.

Once the reconstructed image was consistent with the experimentally measured structural properties and composition, the next step was to ensure the extracted network matched the transport properties of the material, as obtained from the image using direct numerical simulation (DNS). Since the image was quite large, it was expedient to perform simulations on smaller sub-sections. Fig. 6 shows representative elementary volume plots for void phase diffusion, ionomer conduction and electron conduction. The results are all expressed as the ratio of the observed flux to that expected in domain with a volume fraction of unity (e.g., open space for gas diffusion). In all three cases it was observed that stable results were obtained for samples larger than 200^3 voxels, so this size was used to perform subsequent studies. Fig. 7 shows the comparison of the extracted networks to the DNS results on the same subsections of the image for each of the three transport processes of interest. Four different subsections were tested to provide an estimate of the standard deviation between locations, indicated by the error bars. Tests were performed along each principal axis as well, but no notable anisotropy was observed. The match between the PNM and the DNS results was excellent in all cases except the through-plane direction of electron conduction in the carbon phase. Interestingly, even though the PNM results were low, the electron resistance in polarization simulations was found to be negligible. Even the relatively low effective conductivity of the carbon phase did not hinder electron transport appreciably because carbon is so highly conductive.

3. Model development

In this section, we describe the different physics involved in the catalyst layer and how they were accounted for in our model. In the following subsection (Sec. 3.1), transport mechanisms, pore-scale physics, and their mathematical description will be presented. Next, the details of the numerical algorithm that was used to solve the nonlinear multiphysics problem will be provided. Since only the cathode was considered in this study, the terms CL and CCL both refer to the catalyst layer at the cathode and are used interchangeably unless anode is explicitly mentioned. The model was developed for steady-state conditions.

3.1. Physics and governing equations

3.1.1. Gas transport in void/ionomer

At the cathode, oxygen enters the cell via the flow channels, then gets distributed through the GDL, and eventually enters the CL. In the CL at the cathode, oxygen diffuses through the void phase, dissolves into the ionomer at the void-ionomer interface, then further diffuses through the ionomer, and finally reacts with protons at the Nafion-Pt interface via the following overall electrochemical reaction:

$$O_2(g) + 4H^+(aq) + 4e^- \leftrightarrow 2H_2O(\ell) \tag{1}$$

Writing a mass balance for the oxygen gas around an arbitrary pore i yields

$$\sum_{j=1}^{Nb_i} m_{ij} = R_i \qquad i = 1, 2, \cdots, N_p^v \tag{2}$$

where N_p^v is the number of pores in the void phase, Nb_i is the number of neighbor pores to pore i, m_{ij} is the mass flow rate of oxygen from pore i to j, which is only due to molecular diffusion, and finally R_i is the net reaction rate of the oxygen gas at pore i. The reaction only occurs at the ionomer-Pt interface and therefore, R_i is zero elsewhere. Assuming 1D transport between adjacent pores, m_{ij} can be described by

$$m_{ij} = G_{ij}(c_i - c_j) \tag{3}$$

where c is concentration, and G_{ij} is the overall diffusive conductance of the conduit consisting of half of pore i, the entire throat ij, and half of pore j, which can be estimated using the resistors-in-series model:

$$\frac{1}{G_{ij}} = \frac{1}{g_i^p} + \frac{1}{g_{ij}^t} + \frac{1}{g_j^p} \tag{4}$$

where g_i^p, g_{ij}^t, and g_j^p are the diffusive conductance of half of pore i, the

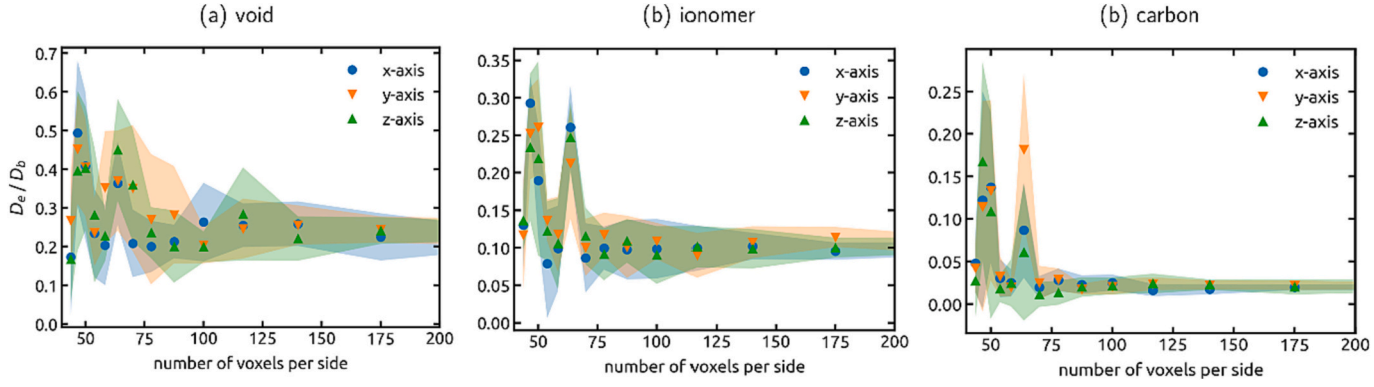

Fig. 6. Representative elementary volume analysis for void, ionomer, and carbon phases along the principal axes using direct numerical simulation of diffusion on the voxel image. Each data point is the average of 8 simulations performed on 8 different cubic sections randomly chosen from the original voxel image. The shaded regions show 1 standard deviation.

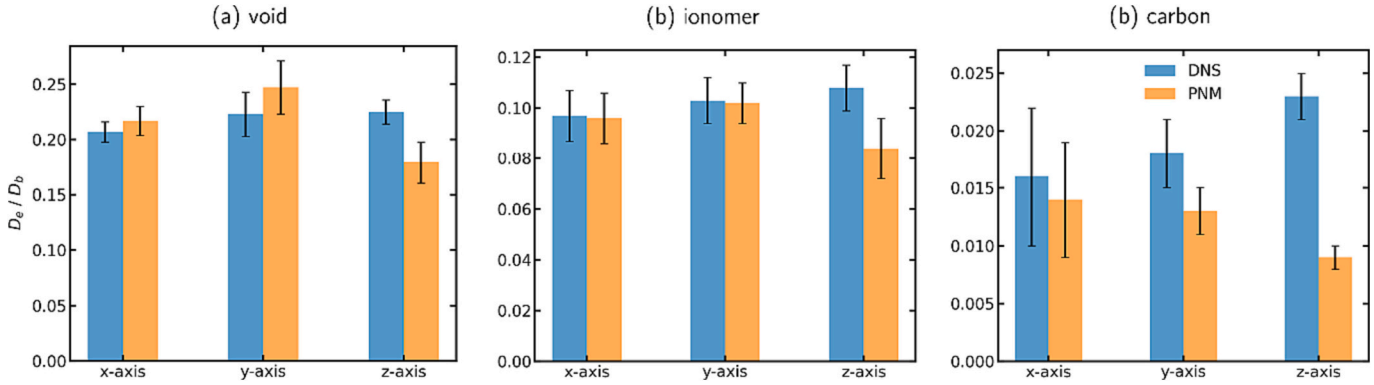

Fig. 7. Comparison of direct numerical simulation predictions on the reconstructed image to the pore network extraction. (a) shows diffusion in the void phase, (b) shows conductions in the ionomer phase, and (c) shows the electron conduction in the carbon phase. Error bars represent the standard deviation of 4 simulations performed on different subsections.

entire throat *ij*, and half of pore *j*, respectively. Based on Fick's first law of diffusion and assuming 1D transport, each of these components can be explicitly calculated using the following generic formula:

$$g \equiv \frac{DA}{\ell} \tag{5}$$

where D is the molecular diffusivity of oxygen in the void phase, A is the cross-sectional area of the half-pore/throat, and finally ℓ is the transport distance. For the throats, the transport distance is the throat length ℓ_{ij}, while for the pores it is pore radius (since transport is assumed to occur from pore center to neighboring pore center).

Since the pore size distribution is in the nanometer range, Knudsen diffusion could significantly hinder transport in the void phase. To account for this effect, the bulk diffusion coefficient of oxygen in air was modified using the formula originally developed by Bosanquet [55], and popularized by Pollard and Present [56] as shown in Eq. (6).

$$D_e = \left(\frac{1}{D_b} + \frac{1}{D_K}\right)^{-1} \tag{6}$$

where D_K is the Knudsen diffusivity, which can be obtained using the self-diffusion coefficient from the kinetic theory of gases as shown in Eq. (7).

$$D_K = \frac{d}{3}\sqrt{\frac{8RT}{\pi MW_{air}}} \tag{7}$$

where d is the pore diameter, and MW_{air} is the molecular weight of air. The value of d is unique to each pore and throat in the network, so the magnitude of the Knudsen effect varies automatically depending on the local sizes.

3.1.2. Electron transport in carbon

Electrons are generated in the CL at the anode where hydrogen is converted to protons and electrons by the following overall reaction:

$$H_2(g) \leftrightarrow 2H^+(aq) + 2e^- \tag{8}$$

and subsequently travels through carbon toward the CL at the cathode where it is consumed in the oxygen reduction reaction (ORR), i.e., Eq. (1). The transport mechanism of electrons was considered to be purely electrical conduction, governed by the Ohm's law. The electrical conductivity of electrons in carbon is on the order of $O(10^3)\ S/m$, which compared to that of protons in the ionomer at about $O(10^0)\ S/m$ is significantly higher. Therefore, it can be safely assumed that the transport of electrons is almost not hindered at all, meaning that the voltage loss in carbon can be neglected, compared to that in the ionomer. Thus, electron transport equations were not solved, and instead a uniform voltage throughout the CL equal to the applied cell voltage at the cathode current collector was considered for each simulation. This feature could be leveraged in future work to study the effect alternative catalyst supports which may have lower conductivity.

3.1.3. Proton transport in the ionomer

Protons, like electrons, are generated in the CL at the anode via the electrochemical reaction described by Eq. (8). Then, they conduct through the ionomer toward the CCL where they react with the solubilized oxygen at the ionomer-Pt interface via the ORR reaction. Like electrons, the transport mechanism of protons through the ionomer was considered to be purely conductive which can be described by Ohm's law. To derive the discretized form of this equation for each pore in the PNM, one could write a charge balance around the arbitrary pore i, which reads as

$$\sum_{j=1}^{Nb_i} q_{ij} = j_i \qquad i = 1, 2, \cdots, N_p^e \tag{9}$$

where N_p^e is the number of pores (nodes) in the electrolyte (ionomer) phase, q_{ij} is the charge flow rate from pore i to j, and j_i is the net rate of charge generation (or simply the net current) at pore i. Since the electrochemical reaction only occurs at the ionomer-Pt interface, j_i is zero except for the Pt nodes. The details on how j_i was calculated will be explained in Sec. 3.1.5. Assuming 1D transport between adjacent pores, q_{ij} can be described by

$$m_{ij} = \sigma_{ij}\left(\phi_i^\ell - \phi_j^\ell\right) \tag{10}$$

where ϕ^ℓ is electrolyte voltage, and σ_{ij} is the overall electrical conductance of the conduit consisting of half of pore i, the entire throat ij, and half of pore j, which can be estimated using the resistors-in-series model as follows:

$$\frac{1}{\sigma_{ij}} = \frac{1}{\sigma_i^p} + \frac{1}{\sigma_{ij}^t} + \frac{1}{\sigma_j^p} \tag{11}$$

where σ_i^p, σ_{ij}^t, and σ_j^p are the electrical conductance of half of pore i, the entire throat ij, and half of pore j, respectively. Based on Ohm's law and assuming 1D transport, each of these components can be explicitly calculated using the following generic formula:

$$\sigma \equiv \frac{\widehat{\sigma} A}{\ell} \tag{12}$$

where $\widehat{\sigma}$ is the electrical conductivity of protons in the ionomer, A is the cross-sectional area of the half-pore/throat, and finally ℓ is the transport distance (e.g., pore radius, which is $d/2$, for the half-pore).

3.1.4. Partitioning of oxygen at void-ionomer interface

For oxygen to participate in the ORR reaction, it first needs to partition into the ionomer at the void-ionomer interface as shown schematically in Fig. 8. The overall diffusive resistance of an arbitrary void-ionomer conduit consists of two components: (1) the resistance from the center of the void pore to the void-ionomer interface, and (2) the resistance from the interface to the center of the ionomer pore. Here, we derive the generic mass flow rate equation for an arbitrary conduit, i.e., pore i | throat ij | pore j. For simplicity, it was assumed that the phase interface is located exactly at the middle of the throat.

It can be shown that the mass flow rate in this case can be calculated using the following formula:

$$m_{ij} = \widehat{G}_{ji}\left(c_i - H_{ij}c_j\right) \tag{13}$$

where H_{ij} is the dimensionless Henry's constant defined as the concentration ratio c_i^*/c_j^* at the interface, and $\widehat{G}_{ji}$ is defined as follows:

$$\frac{1}{\widehat{G}_{ji}} = \left(\frac{1}{g_i^p} + \frac{0.5}{g_{ij}^t}\right) + H_{ij}\left(\frac{1}{g_j^p} + \frac{0.5}{g_{ij}^t}\right) \tag{14}$$

The details of this derivation can be found in the appendix. It is important to note that for the case of interface mass transport, the form of the equation for mass flow rate, i.e., Eq. (13), is asymmetric unlike for the case of single-phase, i.e., Eq. (3). Consequently, when assembling the equations in the matrix form, the A matrix will inevitably be asymmetric. This is important since specialized iterative solvers such as the conjugate gradient (CG) methods can no longer be used.

3.1.5. Butler-Volmer kinetic coupling

At the ionomer-Pt interface, oxygen reacts with protons via the electrochemical reaction given by Eq. (1) to form water. Butler-Volmer kinetics was used to determine the rate of this reaction. Accordingly, the net current generated in pore i, can be calculated by the following formula [57]:

$$j_i = j_0 A_i \left(\frac{c_i}{c_0}\right)^n \left(exp\left[\frac{\alpha_a z_{rds} F}{RT}\eta\right] - exp\left[-\frac{\alpha_c z_{rds} F}{RT}\eta\right]\right) \tag{15}$$

where j_0 is the exchange current density, A_i is the reaction surface area (ionomer-Pt interfacial area), c_i is the concentration of oxygen in pore i, c_0 is the reference concentration, n is the kinetic rate order usually taken to be 1, α_a and α_c are the anodic and cathodic transfer coefficients, respectively, z_{rds} is the number of electrons transferred in rate-determining redox reaction, F is the Faraday's constant, R is the universal gas constant, T is temperature, and η is activation overpotential which can be calculated using the following equation:

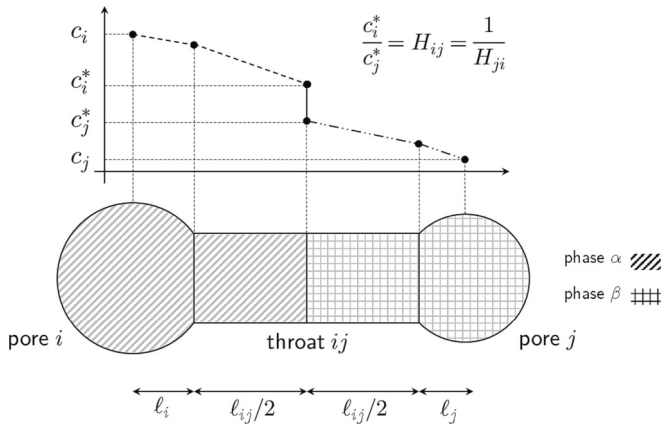

Fig. 8. Mass partitioning at the phase interface between two adjacent pores in a generic pore network model. The phase interface is assumed to be at halfway through the connecting throat.

$$\eta = \phi_s - \phi_\ell - E_{eq} \tag{16}$$

where ϕ_s is the solid phase voltage, ϕ_ℓ is the electrolyte voltage, and E_{eq} is the open-circuit voltage of the redox reaction, which was assumed to be constant and equal to 1.2 V. The local reaction rate of oxygen at each pore, R_i, which is required in the governing equation for mass transport (Eq. (2)), can be directly calculated from the local current generated at pore i (j_i) via the following relationship:

$$R_i = \frac{j_i}{zF} \tag{17}$$

where z is the number of electrons transferred in the overall reaction.

3.1.6. Mass/charge transport in the GDL/membrane

The CCL is sandwiched between the GDL from the cathode side and the membrane from the anode side. Since the focus of this study is multiscale modeling of the CL, the GDL and the membrane were not studied at pore scale. Instead, they were treated as two resistors with fixed conductance values, which were added to the PNM of the CL as two separate resistors, i.e., two pores connected with a throat. The GDL was then connected to the void/ionomer nodes at the GDL-CL interface. Similarly, the membrane was connected to the ionomer nodes at the CL-membrane interface. We assumed that the contact between the CL and the GDL/membrane was ideal, so the diffusive/electrical conductance of these interface throats were set to an arbitrarily large number, so they do not impose any resistance. Fig. 9 shows a schematic diagram of the GDL | CCL | membrane assembly.

3.2. Solution algorithm

To solve the nonlinear multiphysics problem presented in Sec. 3.1, an iterative scheme based on Newton's method was used. The mass transport and the proton/electron transport are coupled via the Butler-Volmer kinetics, which depends on the concentration of oxygen, c_i, the electrolyte voltage, ϕ_i^ℓ, and the solid voltage, ϕ_i^s. A simple iterative scheme based on a weak coupling of these physics was used to deal with the coupling, which is outlined as a flowchart in Fig. 10. Briefly, given an applied cell voltage at which the fuel cell operates, the oxygen transport was solved using a linear solver, assuming a guessed value for the overpotential, η, to obtain an initial concentration profile for oxygen in the void and ionomer phases. Using the obtained values for concentration, the reaction rate computed by Eq. (15) was updated. Using the updated rate, the proton and electron transport were solved using a Newton-based nonlinear solver to obtain the electrolyte and solid-phase voltages, ϕ^ℓ, and ϕ^s, respectively. The overpotential, η, was then updated using the most recent voltage values, and this cycle was repeated until the residual for all three solvers was sufficiently small.

4. Results and discussion

4.1. Model validation

To validate the developed pore network model, we compared the polarization curve from simulation with that from experiment, as shown in Fig. 11. Evidently, the model accurately captured the polarization curve obtained from the experiment. Table 1 shows a summary of the parameters used in the simulations. Unlike continuum volume-averaged models, where there are numerous tuning parameters that can be used to match experimental data, we were able to accomplish this by using the volumetric image as the only input with only the exchange current density j_0 as a free parameter, and even this was well in line with literature values. This achievement is significant since it demonstrates that the macroscopic behavior of such a complex system can be predicted with sufficient accuracy directly from an image with little fine tuning. It should be conceded, of course, that a range of values can be

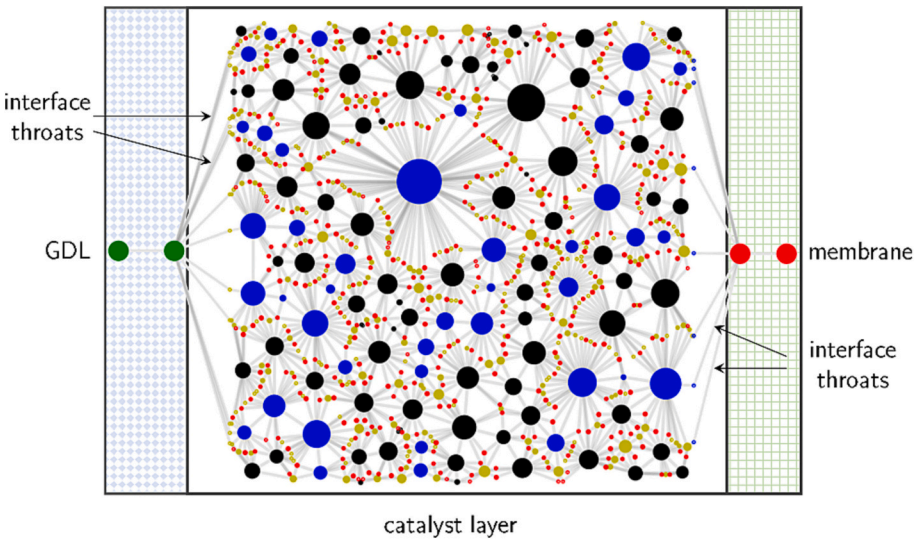

Fig. 9. Schematic diagram of the GDL | CCL | membrane assembly. The resistance of the GDL/membrane were taken into account using a lumped assumption (indicated by large green and red nodes respectively). The diffusive/electrical conductance of the interface throats were set to an arbitrarily large value, so they do not impose any added resistance to the system. Blue nodes are void pores, black nodes are carbon particles, gold nodes are platinum sites, and red nodes are the ionomer network. Connections between all nodes are indicated in grey to avoid over complicating the scene. (For interpretation of the references to colour in this figure legend, the reader is referred to the web version of this article.)

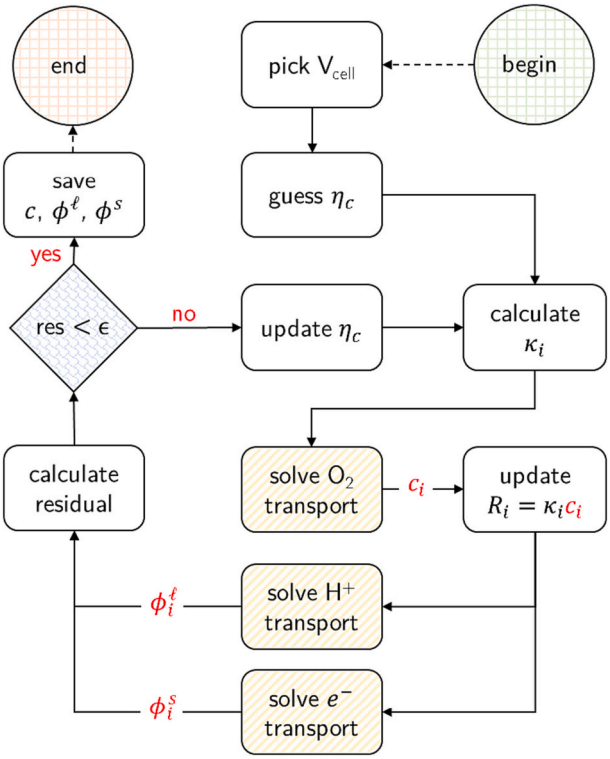

Fig. 10. Flowchart of the numerical algorithm used to solve the governing equations in the CL. Note that the electron transport step was skipped since the voltage loss occurring in the carbon phase was found to be negligible.

obtained for many of the parameters in Table 1 depending on which literature source is used. An effort has been made to use accepted values from reliable sources, but the sensitivity of the present model to these choices is worth examining in future work. Finally, note that the results shown in Fig. 11 validate the model under beginning of life (BOL) conditions. To ensure this was not merely coincidental, the model was further validated throughout cycling, which will be elaborated upon in

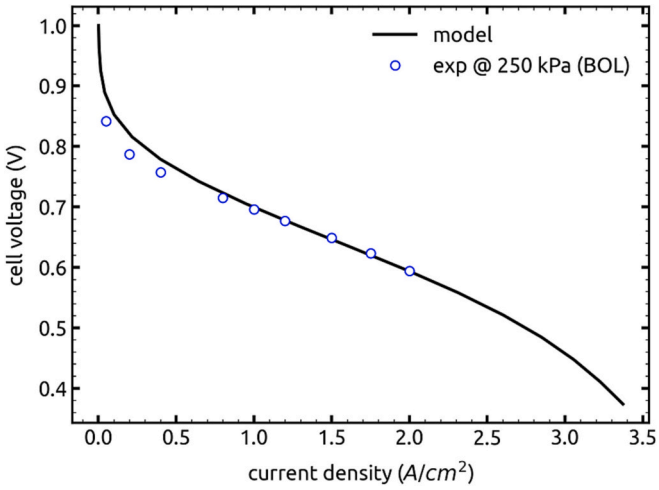

Fig. 11. Polarization curve obtained from the model compared with experimental data [48].

Section 4.2.

4.2. Degradation modeling

While performance of energy storage devices including fuel cells have dramatically improved over the past two decades, extending durability is emerging as the primary challenge if PEMFCs are to displace diesel engines in commercial transport trucks [62,63]. To address durability, it would be very helpful to have a model which could simulate the effects of long-term cycling to help circumvent the need for time-consuming testing. There have been some insightful experimental studies about the effects ECSA loss in catalyst layer electrode [64], but to the best of our knowledge, very few theoretical studies have attempted to model this critical phenomenon. Here we explore two possible ways to include this effect, one simple and one more realistic. In the first case, Pt sites were randomly removed from the domain in proportion to the experimentally observed ECSA loss. The results in Fig. 13(a) show the impact of uniformly deleting 64% and 76% of Pt sites corresponding to

Table 1
Parameters and their values used in this study.

Parameter	Description	Value	Units	Reference
$D^v_{O_2}$	Diffusivity of O_2 in air	Fuller correlation	m^2/s	[58]
$D^e_{O_2}$	Diffusivity of O_2 in ionomer	7.0×10^{-10}	m^2/s	[59]
σ	Ionic conductivity of H^+ in ionomer	5.5	S/m	[54]
α_a	Transfer coefficient of the anode	1.0	–	[60,61]
α_c	Transfer coefficient of the cathode	0.95	–	[60,61]
n	Kinetic rate order	1	–	–
j_0	Exchange current density	1.5×10^{-1}	A/m^2	–
V_{oc}	Open-circuit voltage of the overall reaction	1.2	V	–
V_{mem}	Membrane voltage at the anode CL interface	0	V	–
z	Number of e^- transferred in the overall reaction	4	–	–
z_{rds}	Number of e^- transferred in the rate-determining step	1	–	–
T	Temperature	367.15	K	[48]
p_{tot}	Total pressure	250,000	Pa	[48]
$x^{in}_{O_2}$	Mole fraction of O_2 at inlet	0.21	–	[48]
t_{GDL}	Thickness of the GDL	270	μm	[48]
t_{mem}	Thickness of the membrane	20	μm	[48]
t_{CCL}	Thickness of the CCL	6.4	μm	[48]
δ	Voxel resolution	4	nm	–

ECSA loss after 10 k and 30 k cycles, respectively. Although this captured the qualitative trends, the simulated performance was better than the experimental cases. A second approach was thus considered, which took into account the fact that increased Pt loss was observed near the membrane after cycling [48], which has also been observed in prior studies [65,66]. This is generally attributed to diffusion of dissolved Pt^{2+} into the membrane, where it is then reduced by crossover H_2 [67]. To build on these findings, the data have been further analyzed here to obtain an ECSA profile. Fig. 12a shows a cross-sectional TEM image of the cathode after 30,000 voltage cycles, from which local Pt concentration was obtained by energy-dispersive X-ray spectroscopy (EDXS).

Fig. 12b shows the Pt mass profile normalized to the highest value across the cathode. Integration of the Pt mass profile in Fig. 12b revealed that only 15% Pt of the original mass was lost after 30 k cycles despite an 80% reduction in ECSA. This mass was preferentially lost near the membrane with little to no loss of Pt mass further away from the membrane. The relatively small Pt loss compared to ECSA loss, suggest that dissolved Pt^{2+} undergoes redeposition onto existing Pt particles (Ostwald ripening), leading to larger agglomerated particles with less available surface area. This assertion is validated by looking at particle diameter measurements from the TEM, which revealed that the average sizes had increased from $d_{\mathrm{BOL}} = 4.1 \pm 1.6\ nm$ to $d_{30k} = 14.6 \pm 6.8\ nm$, using volume weighted diameters [68]. In Fig. 12c, the Pt mass distribution, including the particle size changes, was converted to ECSA distribution the following expression, adopted from Chen et al. [66]:

$$ECSA_{30k} = ECSA_{BOL} \times \frac{d_{30k}}{d_{BOL}} \times \%m_{Pt(30k)} \tag{18}$$

The estimated ECSA at 30 k cycles in Fig. 12c varies from 24 m^2/g_{Pt} next to the GDL to 13 m^2/g_{Pt} next to the membrane. The average ECSA across the cathode was 20.3 m^2/g_{Pt}, in good agreement with the experimentally measured value (indicated by the dashed lines).

Accordingly, the degradation process was incorporated in the present PNM model by removing a fraction of Pt nodes according to a probability distribution proportional the Pt ECSA profile shown in Fig. 12c. For this proof-of-concept analysis, the Pt ECSA profile at EOL (i.e., 30 k cycles) was used for 10 k cycles since TEM intensity tomograms for this sample were not available, though fewer nodes were deleted to match the experimental measured overall ECSA after 10 k cycles. A more realistic approach would have been to use the average of BOL and EOL. However, as can be seen in Fig. 13(b) a satisfactory prediction of performance loss was obtained. This result shows that the model has captured both the qualitative and the quantitative trend seen in the experimental data reasonably well, given the simplicity of the degradation procedure presented here. Note that here we approximated both the Pt loss and agglomeration process by removing Pt nodes to match the equivalent ECSA loss and profile. A more realistic approach would be to explicitly model this process, i.e., dissolution, diffusion/migration, and redeposition, which would capture the change in ECSA due to cycling and could possibly lead to a better match with the experimental data. This is a subject for future work but based on the success of the simple method used here, seem to show promise.

4.3. Significance of the Knudsen diffusion

Due to the small pore sizes present in typical catalyst layers, it is expected that the Knudsen effect should hinder gas transport. Experimental work by Kim and Gostick [69], for instance, observed that the contribution of the Knudsen effect to the observed effective gas diffusivity was substantial (resulting in a 2-5× increase in tortuosity). In many modeling studies of the fuel cell catalyst layer, Knudsen diffusion is considered to be important and therefore it is included in the modeling formulation [36,41,70,71]. In this study, however, it was found not to be the case. Fig. 14a shows three pairs of polarization curves at BOL, 10 k and 30 k cycling conditions, with and without considering the Knudsen

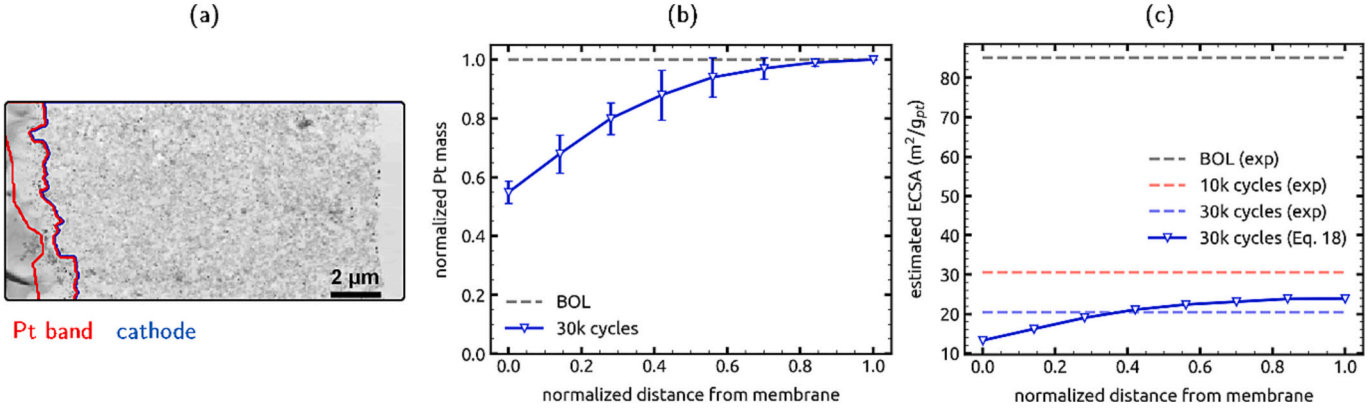

Fig. 12. (a) Cross-sectional TEM image of cathode after 30,000 cycles, (b) Pt mass profile measured by EDXS, and (c) calculated ECSA profile. The dashed lines in (c) are experimentally measured average ECSA values for the entire cathode, whereas the blue solid line is the calculated ECSA profile based on Eq. (18). (For interpretation of the references to colour in this figure legend, the reader is referred to the web version of this article.)

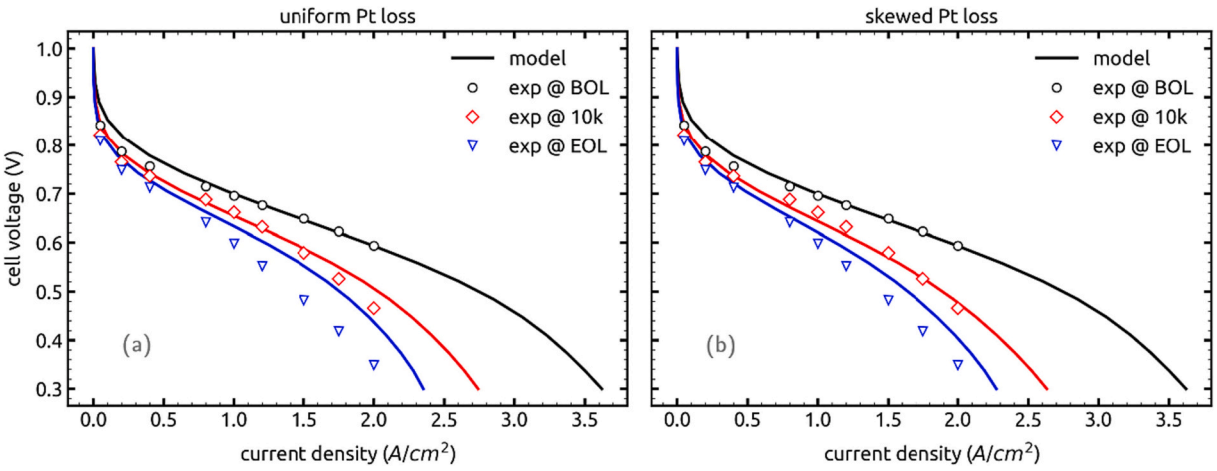

Fig. 13. Polarization curves obtained from the model at the beginning of life (BOL) condition, and after 10 k and 30 k cycles, compared with experimental data obtained under the same conditions [68]. **(a)** Pt sites were removed randomly based on a uniform distribution to achieve the desired ECSA for each cycling scenario. **(b)** Pt sites were removed randomly based on a nonuniform distribution proportional to the experimental Pt mass profiles calculated from TEM intensity images.

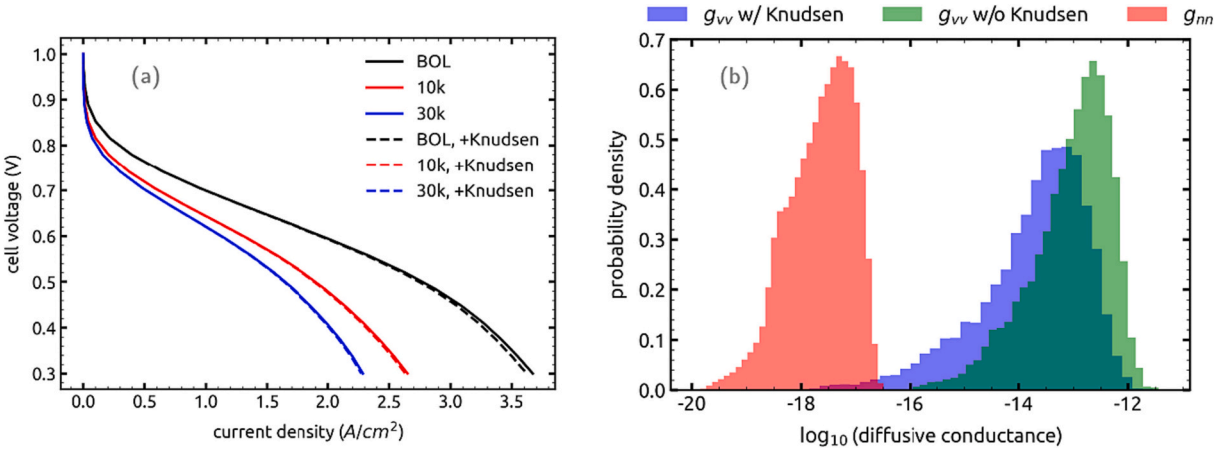

Fig. 14. (a) Polarization curves with and without the Knudsen diffusion at BOL, 10 k, and 30 k cycling, and (b) histogram of the diffusive conductance of void-void and ionomer-ionomer throats (connections) in the pore network model, with and without considering the Knudsen diffusion. Since the Knudsen diffusion mostly affects the gas phase, the diffusive conductance of the ionomer-ionomer connections is not shown here for clarity.

diffusion. This figure shows that the polarization behavior of the catalyst layer is almost unaffected by the Knudsen effect. Based on this figure, the maximum error in the predicted current occurs at the BOL condition at 0.3 V and is <2%. The reason for this is that the resistance of oxygen transport in the ionomer phase is 3–4 orders of magnitude higher than that in the void phase, and the presence of Knudsen diffusion only attenuates it by at most one order of magnitude. Fig. 14b shows the histogram of the diffusive conductance of the void-void and ionomer-ionomer throats (connections) in the pore network model, with and without considering the Knudsen diffusion. Note that since the Knudsen diffusion mostly affects the gas phase species, the diffusive conductance of the ionomer phase remains unchanged and therefore, it is not shown in the figure. Based on this figure, although considering the Knudsen diffusion does significantly decrease the diffusive conductance of the gas phase, because of the huge gap between the diffusivity of oxygen in the gas phase and in the ionomer, the "overall" transport inside the catalyst layer is still dominated by the resistance of the ionomer phase, and therefore it is unaffected by Knudsen diffusion. In fact, studies citing Knudsen diffusion to play an important role in modeling the catalyst layer have studied this effect in isolation, i.e., how it affects the effective diffusivity of the catalyst layer, which indeed significantly decreases. The scope of those studies is either limited to finding effective properties, or those studying fuel cell polarization often do not report the results without considering the Knudsen effect and consequently, Knudsen effects have been widely accepted to be an important parameter in modeling fuel cell performance. However, as shown in this study, the effective diffusivity of the catalyst layer does not significantly impact the overall transport and therefore, the Knudsen effect can be safely neglected when studying the overall performance of the fuel cell.

This finding is further confirmed by looking at the concentration scatter plot for oxygen in the void phase as shown in Fig. 15 plotted at different cell voltages in presence of the Knudsen effect. Based on this figure, the oxygen concentration in the void phase almost remains constant along the CL thickness, even at relatively high overpotentials (ex. $V_{cell} = 0.5\ V$). This implies that mass transfer resistance in the void phase is negligible, which confirms that the Knudsen effect does not significantly change the polarization curves. Another interesting feature of this figure is that as the overpotential increases, the spread of the distribution of oxygen concentration in the void phase increases, which is expected since the electrode undergoes a higher reaction rate. Furthermore, the width of the spread progressively increases toward the membrane from the GDL, indicating that the ORR reaction mostly occurs near the membrane.

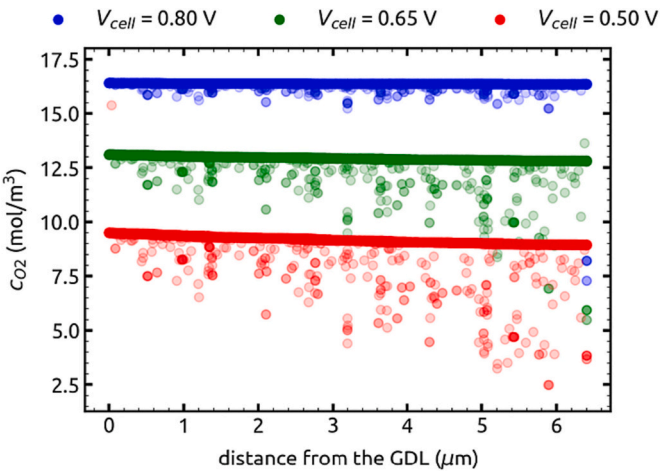

Fig. 15. Concentration scatter plot for c_{O_2} in the void phase vs. the distance from the GDL at BOL condition.

4.4. Effect of water saturation

Given the small effect that gas phase diffusion had on performance discussed in the previous section, it was next explored what impact liquid water in the void space might have. For this study the generation of liquid water was not included in a rigorous way, since that would justify a separate study on its own, but was instead approximated by assigning a randomly selected fraction of void pores to be water-filled. Due to the low solubility and low diffusion coefficient of oxygen in water, combined with the comparatively the long transport lengths in the void pores (compared to the ionomer pores), it was assumed that these water-filled pores had negligible diffusive conductance to oxygen. The volume fraction, or saturation, of water-filled pores was varied between 0 and 0.5, and polarization curves were simulated using the same conditions and parameters as the BOL simulations described above. The results are shown in Fig. 16a. It is evident from this figure that the performance did not significantly change even up to flooding the electrode with 30% liquid water, which further supports the findings from the previous section that void phase transport in the CL does not noticeably limit the overall performance.

Beyond 30% saturation there appears a noticeable drop in performance. This is caused by percolation effects in the network, which have several knock-on effects that are worth dissecting. Firstly, some air-filled pores are surrounded by water clusters so have no access to the oxygen. These pores are effectively water-filled since they cannot support any reaction. The secondary y-axis in Fig. 16(b) reports the apparent saturation, which is the sum of both water-filled and water-surrounded pores, showing the nearly 40% of the pores can be effectively inactive before a noticeable performance hit is incurred. It should be noted that these values are approximations only since the water configuration was not generated in a physically rigorous manner and, moreover, the domain is narrow so finite-size effects will impact the percolation behavior.

A second effect of percolation is that the accessible pores are increasingly likely to be found near the GDL interface as saturation increase. The has the effect of shifting the reaction zone toward the GDL interface since that is where the oxygen filled pores are located. Fig. 17 shows two-dimensional histograms of local reaction rate at individual Pt sites as a function of the distance from the GDL for various water saturations at $V_{\text{cell}} = 600\,mV$ overlaid with the corresponding cumulative reaction rate %. The cumulative % at cross section $z = \delta$ is defined as the net reaction rate within δ microns from the GDL divided by the total reaction rate in the entire electrode. Based on this figure, from 0 to 30% water saturation the reaction is mostly happening near the membrane with ~60% of the net reaction rate occurring within 2 μm from the membrane. This is expected since percolation pathways from the GDL to membrane are abundant at these water saturations, so the oxygen from the GDL can reach the membrane with almost no drop in concentration where it reacts with the incoming protons. As the saturation increases, this trend reverses, causing the reaction front to move closer to the GDL. Based on this figure, at 60% water saturation most of the reaction is happening close to the GDL with almost 90% of the net reaction rate occurring within 1 μm from the GDL. Under such high saturations, there no longer exists a percolating gas pathway between the GDL and the membrane as previously shown in Fig. 16b. Consequently, protons need to travel much further from the membrane to reach the oxygen gas near the GDL. This added transport length increases the ohmic loss, which also manifests itself by the greater slope of the polarization curve in the ohmic loss region in Fig. 16a.

4.5. Computational time

As discussed in the Introduction, an important aspect to consider in pore-scale simulations is the computational time. One of the main reasons to conduct pore-scale simulations is their ability to predict macroscopic behavior as a result of change in microstructure or pore-

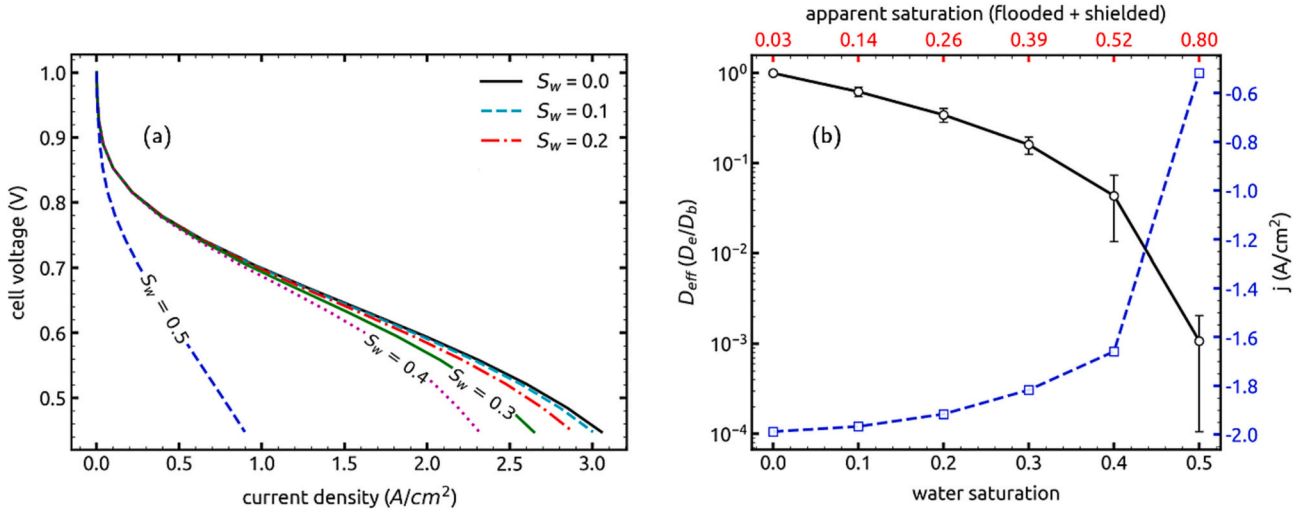

Fig. 16. (a) Polarization curves for various water saturations, simulated by randomly removing a fraction of void pores, and (b) effective diffusivity of the catalyst layer as a function of water saturation, overlaid with the corresponding current density at $V_{cell} = 600\,mV$.

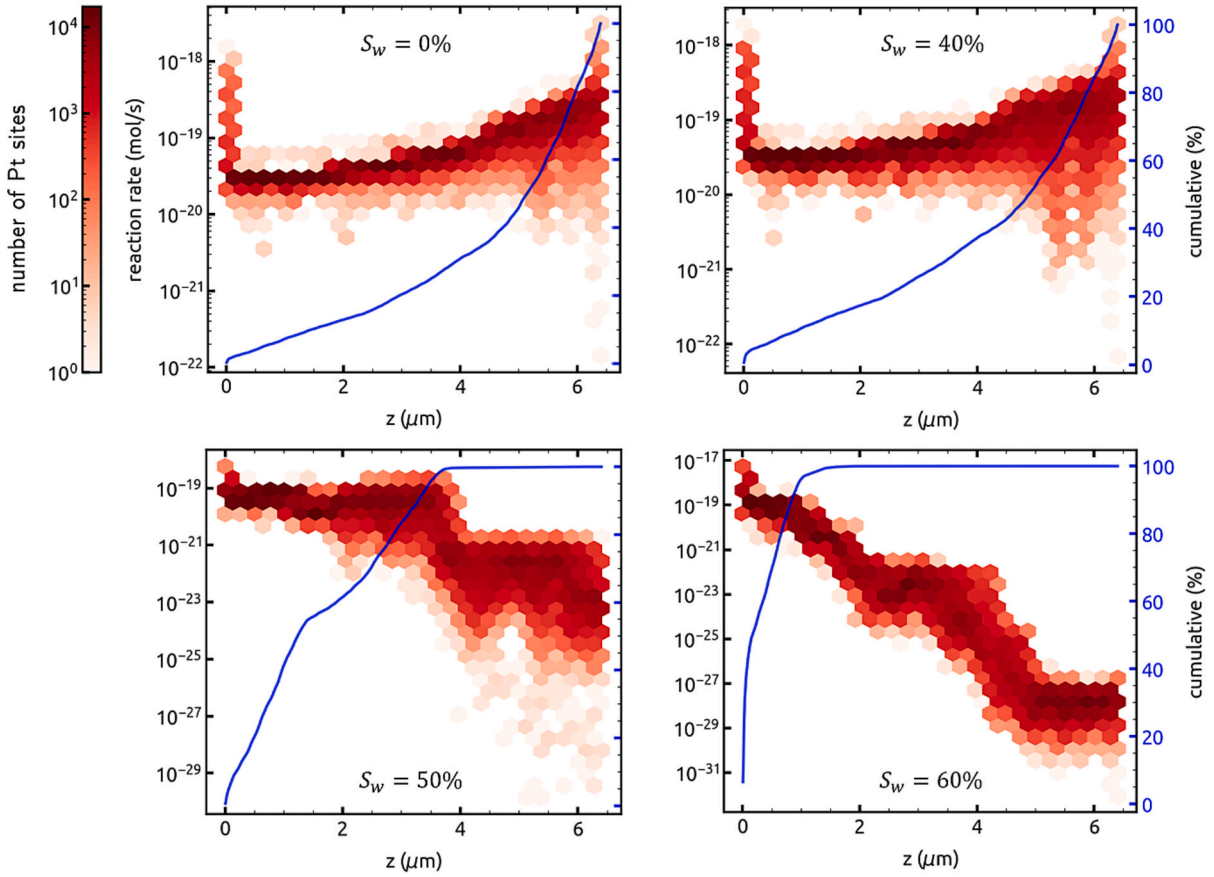

Fig. 17. Two-dimensional histograms of local reaction rate at individual Pt sites as a function of distance from GDL for various water saturations at $V_{cell} = 600\ mV$ overlaid with the corresponding cumulative reaction rate %. The cumulative % at each cross section $z = \delta$ is defined as the net reaction rate within δ microns from the GDL divided by the total reaction rate in the entire electrode.

scale physics and therefore, they could potentially be used in an optimization process to design better electrodes. However, due to the excessive computational cost of pore-scale models, this has not been realized and most pore-scale studies have focused on conducting a pore-scale simulation at a set of fixed operating parameters. Fig. 18 shows the computational cost of similar pore-scale studies of the catalyst layer vs. the domain size. Based on this figure, it takes hours (to days) to conduct a pore-scale simulation of the catalyst layer at a single voltage on a powerful desktop workstation. To explore the space of possible microstructures and other pore-scale parameters (e.g., Pt/ionomer loading, etc.) it requires generating tens of thousands of such data points. Therefore, using traditional pore-scale numerical methods is simply not feasible. Using the pore network model approach developed and validated in this study, one can generate the entire polarization curve (which consists of 15 to 20 voltage data points) on the order of minutes, which is at least two orders of magnitude faster than other methods, making it an ideal candidate to be used for in silico microstructural optimization.

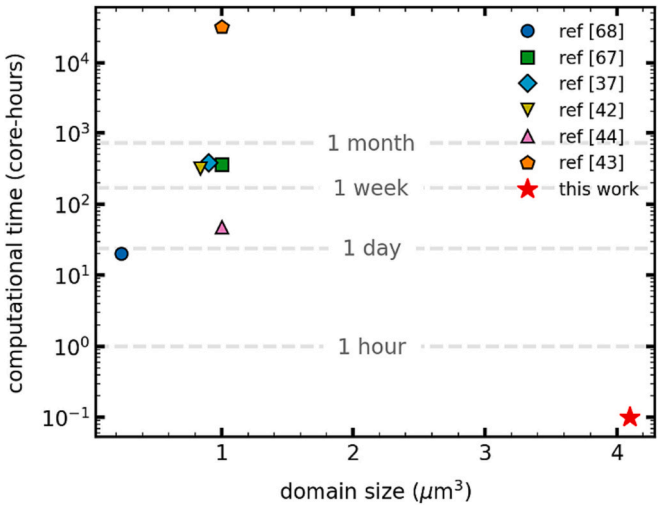

Fig. 18. Computational cost of similar pore-scale studies of the catalyst layer [38,43–45,72,73] vs. the domain size. Each data point refers to a pore-scale simulation for a single-voltage.

5. Conclusion

In this study, a multiscale, multiphase, and multiphysics pore network model of the fuel cell catalyst layer was developed that was able to describe the overall polarization behavior of a PEM fuel cell. The model was developed based on volumetric image data of a standard Pt/V electrode [48]. This study is, to the best of our knowledge, the first pore network model of the CL where all four phases, namely void, carbon, ionomer, and platinum have been accounted for as separate phases. The low computational cost of the PNM approach enabled the modeling of a reasonably large cross-section ($\sim 1\ \mu m^2$) of the electrode, and the entire thickness of the electrode ($\sim 6.4\ \mu m$), which sets a new milestone for pore-scale studies. The developed model was shown to agree with the experimental data of the same electrode from which the network model was extracted. Given that exchange current density was the only free parameter used for fitting, this work speaks to the advantage of pore network modeling not just for qualitative analysis, but as a tool to

predict the structure-performance relationship of CLs. Moreover, using the developed model it was possible to incorporate the effects of Pt degradation and obtain a reasonably satisfactory match to experimental data for EOL conditions. This agreement was even better when Pt mass profile after cycling (obtained from TEM intensity tomograms) was used to remove Pt sites rather than uniform removal, suggesting that a transient model which includes more rigorous Pt dissolution thermodynamics and kinetics has the potential to simulate degradation and augment accelerated stress testing. In addition, it was shown that the Knudsen diffusion does not play a significant role in transport of oxygen in the CL and therefore most of the mass transfer resistance was in the ionomer phase. It was found that at the worst case (close to the limiting current regime), excluding the Knudsen diffusion would only overestimate the generated current by 2–3%. Another interesting finding was that regardless of the voltage at which the cell operates, the concentration of oxygen in the void phase is practically constant across the thickness of the CL due to the rapid diffusion into the macropores compared to transport in the ionomer phase. This finding highlights the fact that the ionomer is the transport bottleneck and consequently future studies should focus on making electrodes with better ionomer management [74]. Lastly, the impact of liquid water in the void pores was explored by randomly assigning pores as water-filled and thus impassible by oxygen. Not until over 30% water saturation was reached was the performance noticeably impacted, due to the high transport rates of oxygen in the available pores. Beyond 30% the performance dropped rapidly, due to the water blockages causing percolation effects in the void phase. At higher saturation the reaction shifts almost entirely to the CL-GDL interface since oxygen is unable to penetrate into the CL domain.

CRediT authorship contribution statement

Mohammad Amin Sadeghi: Writing – review & editing, Writing – original draft, Visualization, Validation, Software, Methodology, Investigation, Formal analysis, Data curation. **Zohaib Atiq Khan:** Software, Methodology, Investigation, Data curation, Conceptualization. **Mehrez Agnaou:** Software, Methodology, Investigation. **Leiming Hu:** Writing – original draft, Software, Investigation, Data curation. **Shawn Litster:** Supervision, Resources, Project administration, Funding acquisition, Conceptualization. **Anusorn Kongkanand:** Writing – original draft, Funding acquisition, Formal analysis, Data curation. **Elliot Padgett:** Investigation, Formal analysis, Data curation. **David A. Muller:** Supervision, Resources, Project administration, Funding acquisition. **Tomislav Friscic:** Writing – original draft, Project administration, Funding acquisition. **Jeff Gostick:** Writing – review & editing, Writing – original draft, Validation, Supervision, Software, Resources, Project administration, Funding acquisition, Formal analysis, Conceptualization.

Declaration of Competing Interest

As the corresponding author I confirm that the authors have no competing interests to declare.

Data availability

Data will be made available on request.

Acknowledgments

The work described here was financially supported by the Natural Science and Engineering Research Council (NSERC) of Canada's Discovery program, CANARIE under project RS3-141, the U.S. Department of Energy, Office of Energy Efficiency and Renewable Energy under grant DE-EE0007271. The electron microscope facilities used at the Cornell Center for Materials Research are supported by the National Science Foundation (MRI-1429155, DMR-1719875, DMR-2039380).

Appendix A. Appendix

Derivation of the mass partitioning equation for pore network models

Consider the conduit consisting of pore i, throat ij, and pore j. Assume pore i is occupied by phase α and pore j is occupied by phase β and that the phase interface is exactly at the center of throat ij, as shown in Fig. 8. Let K_i be the diffusive conductance from the center of pore i to the center of throat ij such that $m_{ij} = K_i(c_i - c_i^*)$. Similarly, let K_j be the diffusive conductance from the center of pore j to the center of throat ij such that $m_{ji} = K_j\left(c_j - c_j^*\right)$. Assuming that the phase interface is at thermodynamic equilibrium governed by the Henry's law, the interface concentrations can be related to each other via the dimensionless Henry's constant $H_{ij} = c_i^*/c_j^*$ or $H_{ji} = c_j^*/c_i^*$.

Given that $m_{ij} = -m_{ji}$, one could solve these equations for the interface concentrations to obtain:

$$c_j^* = \frac{(K_i/K_j)c_i + c_j}{(K_i/K_j)H_{ij} + 1} \tag{19}$$

Substituting Eq. (19) into the formula for m_{ij} and rearranging, one could obtain the following closed formula for m_{ij}:

$$m_{ij} = \frac{1}{\frac{1}{K_i} + \frac{H_{ij}}{K_j}}(c_i - H_{ij}c_j) \tag{20}$$

where the prefactor can further be simplified. Given the definition of K_i, it accounts for the diffusive conductance of half pore i and half throat ij. Since these two resistances are in series, the following simplified formula can be derived for K_i using a resistor-in-series model:

$$\frac{1}{K_i} = \frac{1}{g_i^p} + \frac{0.5}{g_{ij}^t} \tag{21}$$

Likewise, one could obtain a similar formula for K_j as follows:

$$\frac{1}{K_j} = \frac{1}{g_j^p} + \frac{0.5}{g_{ij}^t} \tag{22}$$

The derivation of Eq. (13) is now complete.

References

[1] Panwar NL, Kaushik SC, Kothari S. Role of renewable energy sources in environmental protection: a review. Renew. Sust. Energ. Rev. Apr. 2011;15(3): 1513–24. https://doi.org/10.1016/j.rser.2010.11.037.

[2] Preuster P, Alekseev A, Wasserscheid P. Hydrogen storage technologies for future energy systems. Annu Rev Chem Biomol Eng Jun. 2017;8(1):445–71. https://doi.org/10.1146/annurev-chembioeng-060816-101334.

[3] Inoue G. Secondary batteries and fuel cell systems for next-generation vehicles. In: Kato Y, Koyama M, Fukushima Y, Nakagaki T, editors. Energy technology roadmaps of Japan. Tokyo: Springer Japan; 2016. p. 537–47. https://doi.org/10.1007/978-4-431-55951-1_43.

[4] Gröger O, Gasteiger HA, Suchsland J-P. Review—electromobility: batteries or fuel cells? J. Electrochem. Soc. Jan. 2015;162(14):A2605–22. https://doi.org/10.1149/2.0211514jes.

[5] Wang Y, Chen KS, Mishler J, Cho SC, Adroher XC. A review of polymer electrolyte membrane fuel cells: technology, applications, and needs on fundamental research. Appl. Energy 2011;88(4):981–1007. https://doi.org/10.1016/j.apenergy.2010.09.030.

[6] Alaswad A, et al. Technical and commercial challenges of proton-exchange membrane (PEM) fuel cells. Energies Dec. 2020;14(1):144. https://doi.org/10.3390/en14010144.

[7] Guandalini G, Campanari S. Well-to-wheel driving cycle simulations for freight transportation: battery and hydrogen fuel cell electric vehicles. In: 2018 International Conference of Electrical and Electronic Technologies for Automotive. Milan: IEEE; Jul. 2018. p. 1–6. https://doi.org/10.23919/EETA.2018.8493216.

[8] Huya-Kouadio J. DOE hydrogen and fuel cells program record. 2017.

[9] Sui P-C, Zhu X, Djilali N. Modeling of PEM fuel cell catalyst layers: status and outlook. Electrochem Energ Rev Sep. 2019;2(3):428–66. https://doi.org/10.1007/s41918-019-00043-5.

[10] Wang Y, Ruiz Diaz DF, Chen KS, Wang Z, Adroher XC. Materials, technological status, and fundamentals of PEM fuel cells – a review. Mater. Today Jan. 2020;32: 178–203. https://doi.org/10.1016/j.mattod.2019.06.005.

[11] Bai F, et al. Three-dimensional multi-field digital twin technology for proton exchange membrane fuel cells. Appl. Energy Oct. 2022;324:119763. https://doi.org/10.1016/j.apenergy.2022.119763.

[12] Wang B, Zhang G, Wang H, Xuan J, Jiao K. Multi-physics-resolved digital twin of proton exchange membrane fuel cells with a data-driven surrogate model. Energy AI Aug. 2020;1:100004. https://doi.org/10.1016/j.egyai.2020.100004.

[13] Bernardi DM, Verbrugge MW. A mathematical model of the solid-polymer-electrolyte fuel cell. J. Electrochem. Soc. 1992;139(9):2477. https://doi.org/10.1149/1.2221251.

[14] Broka K, Ekdunge P. Modelling the PEM fuel cell cathode. J. Appl. Electrochem. Mar. 1997;27(3):281–9. https://doi.org/10.1023/A:1018476612810.

[15] Siegel NP, Ellis MW, Nelson DJ, von Spakovsky MR. Single domain PEMFC model based on agglomerate catalyst geometry. J. Power Sources Mar. 2003;115(1):81–9. https://doi.org/10.1016/S0378-7753(02)00622-5.

[16] Schwarz DH, Djilali N. 3D modeling of catalyst layers in PEM fuel cells. J. Electrochem. Soc. Nov. 2007;154(11):B1167. https://doi.org/10.1149/1.2777011.

[17] Sun W, Peppley BA, Karan K. An improved two-dimensional agglomerate cathode model to study the influence of catalyst layer structural parameters. Electrochim. Acta May 2005;50(16):3359–74. https://doi.org/10.1016/j.electacta.2004.12.009.

[18] Gloaguen F, Durand R. Simulations of PEFC cathodes: an effectiveness factor approach. J. Appl. Electrochem. Sep. 1997;27(9):1029–35. https://doi.org/10.1023/A:1018478324564.

[19] Gloaguen F, Convert P, Gamburzev S, Velev OA, Srinivasan S. An evaluation of the macro-homogeneous and agglomerate model for oxygen reduction in PEMFCs. Electrochim. Acta Aug. 1998;43(24):3767–72. https://doi.org/10.1016/S0013-4686(98)00136-4.

[20] Jaouen F, Lindbergh G, Sundholm G. Investigation of mass-transport limitations in the solid polymer fuel cell cathode : I. Mathematical model. J. Electrochem. Soc. Mar. 2002;149(4):A437. https://doi.org/10.1149/1.1456916.

[21] Yin K-M, Cheng B-S, Chiang K-W. Non-uniform agglomerate cathode catalyst layer model on the performance of PEMFC with consideration of water effect. Renew. Energy Sep. 2016;95:191–201. https://doi.org/10.1016/j.renene.2016.04.015.

[22] Li S, Yuan J, Xie G, Sundén B. Effects of agglomerate model parameters on transport characterization and performance of PEM fuel cells. Int. J. Hydrog. Energy Apr. 2018;43(17):8451–63. https://doi.org/10.1016/j.ijhydene.2018.03.106.

[23] Li X, et al. Simulation on cathode catalyst layer in proton exchange membrane fuel cell: sensitivity of design parameters to cell performance and oxygen distribution. Int. J. Hydrog. Energy 2022;47(58):24452–63.

[24] Sánchez-Ramos A, Gostick JT, García-Salaberri PA. Modeling the effect of low Pt loading cathode catalyst layer in polymer electrolyte fuel cells: Part I. Model formulation and validation. J. Electrochem. Soc. Dec. 2021;168(12):124514. https://doi.org/10.1149/1945-7111/ac4456.

[25] Sánchez-Ramos A, Gostick JT, García-Salaberri PA. Modeling the effect of low Pt loading cathode catalyst layer in polymer electrolyte fuel cells. Part II: Parametric analysis. J. Electrochem. Soc. Jul. 2022;169(7):074503. https://doi.org/10.1149/1945-7111/ac811d.

[26] Sabharwal M, Pant LM, Putz A, Susac D, Jankovic J, Secanell M. Analysis of catalyst layer microstructures: from imaging to performance. Fuel Cells Dec. 2016; 16(6):734–53. https://doi.org/10.1002/fuce.201600008.

[27] Sabharwal M, Pant LM, Patel N, Secanell M. Computational analysis of gas transport in fuel cell catalyst layer under dry and partially saturated conditions. J. Electrochem. Soc. 2019;166(7):F3065–80. https://doi.org/10.1149/2.0081907jes.

[28] Antoine O, Bultel Y, Durand R, Ozil P. Electrocatalysis, diffusion and ohmic drop in PEMFC: particle size and spatial discrete distribution effects. Electrochim. Acta Aug. 1998;43(24):3681–91. https://doi.org/10.1016/S0013-4686(98)00126-1.

[29] Sui P-C, Chen L-D, Seaba JP, Wariishi Y. Modeling and optimization of a PEMFC catalyst layer. SAE Trans. 1999;108:729–37.

[30] Yeong CLY, Torquato S. Reconstructing random media. Phys. Rev. E Jan. 1998;57 (1):495–506. https://doi.org/10.1103/PhysRevE.57.495.

[31] Mukherjee PP, Wang C-Y. Stochastic microstructure reconstruction and direct numerical simulation of the PEFC catalyst layer. J. Electrochem. Soc. May 2006; 153(5):A840. https://doi.org/10.1149/1.2179303.

[32] Kim SH, Pitsch H. Reconstruction and effective transport properties of the catalyst layer in PEM fuel cells. J. Electrochem. Soc. Jun. 2009;156(6):B673. https://doi.org/10.1149/1.3106136.

[33] Rong F, Huang C, Liu Z-S, Song D, Wang Q. Microstructure changes in the catalyst layers of PEM fuel cells induced by load cycling. J. Power Sources Jan. 2008;175 (2):699–711. https://doi.org/10.1016/j.jpowsour.2007.10.006.

[34] Liu X, et al. 3D generation and reconstruction of the fuel cell catalyst layer using 2D images based on deep learning. J. Power Sources Adv. Mar. 2022;14:100084. https://doi.org/10.1016/j.powera.2022.100084.

[35] Chen L, Kang Q, Tao W. Pore-scale study of reactive transport processes in catalyst layer agglomerates of proton exchange membrane fuel cells. Electrochim. Acta May 2019;306:454–65. https://doi.org/10.1016/j.electacta.2019.03.158.

[36] Chen L, Zhang R, Kang Q, Tao W-Q. Pore-scale study of pore-ionomer interfacial reactive transport processes in proton exchange membrane fuel cell catalyst layer. Chem. Eng. J. Jul. 2020;391:123590. https://doi.org/10.1016/j.cej.2019.123590.

[37] Zhang R, He P, Bai F, Chen L, Tao W-Q. Multiscale modeling of proton exchange membrane fuel cells by coupling pore-scale models of the catalyst layers and cell-scale models. Int. J. Green Energy Sep. 2021;18(11):1147–60. https://doi.org/10.1080/15435075.2021.1891912.

[38] Zhang R, Min T, Chen L, Kang Q, He Y-L, Tao W-Q. Pore-scale and multiscale study of effects of Pt degradation on reactive transport processes in proton exchange membrane fuel cells. Appl. Energy Nov. 2019;253:113590. https://doi.org/10.1016/j.apenergy.2019.113590.

[39] Zhang R, Min T, Liu Y, Chen L, Tao W-Q. Pore-scale study of effects of different Pt loading reduction schemes on reactive transport processes in catalyst layers of proton exchange membrane fuel cells. Int. J. Hydrog. Energy Jun. 2021;46(38): 20037–53. https://doi.org/10.1016/j.ijhydene.2021.03.124.

[40] Cetinbas FC, Ahluwalia RK, Kariuki NN, De Andrade V, Myers DJ. Effects of porous carbon morphology, agglomerate structure and relative humidity on local oxygen transport resistance. J. Electrochem. Soc. 2020;167(1):013508. https://doi.org/10.1149/2.0082001JES.

[41] Hou Y, Deng H, Pan F, Chen W, Du Q, Jiao K. Pore-scale investigation of catalyst layer ingredient and structure effect in proton exchange membrane fuel cell. Appl. Energy Nov. 2019;253:113561. https://doi.org/10.1016/j.apenergy.2019.113561.

[42] Shin S, Kim A-R, Um S. Computational prediction of nanoscale transport characteristics and catalyst utilization in fuel cell catalyst layers by the lattice Boltzmann method. Electrochim. Acta Jun. 2018;275:87–99. https://doi.org/10.1016/j.electacta.2018.04.138.

[43] Mu Y-T, Yang S-R, He P, Tao W-Q. Mesoscopic modeling impacts of liquid water saturation, and platinum distribution on gas transport resistances in a PEMFC catalyst layer. Electrochim. Acta Aug. 2021;388:138659. https://doi.org/10.1016/j.electacta.2021.138659.

[44] Chen L, Wu G, Holby EF, Zelenay P, Tao W-Q, Kang Q. Lattice Boltzmann pore-scale investigation of coupled physical-electrochemical processes in C/Pt and non-precious metal cathode catalyst layers in proton exchange membrane fuel cells. Electrochim. Acta Mar. 2015;158:175–86. https://doi.org/10.1016/j.electacta.2015.01.121.

[45] Inoue G, Park K, So M, Kimura N, Tsuge Y. Microscale simulations of reaction and mass transport in cathode catalyst layer of polymer electrolyte fuel cell. Int. J. Hydrog. Energy Mar. 2022;47(25):12665–83. https://doi.org/10.1016/j.ijhydene.2022.02.021.

[46] Wu R, Liao Q, Zhu X, Wang H. Pore network modeling of cathode catalyst layer of proton exchange membrane fuel cell. Int. J. Hydrog. Energy Aug. 2012;37(15): 11255–67. https://doi.org/10.1016/J.IJHYDENE.2012.04.036.

[47] El Hannach M, Prat M, Pauchet J. Pore network model of the cathode catalyst layer of proton exchange membrane fuel cells: analysis of water management and electrical performance. Int. J. Hydrog. Energy Dec. 2012;37(24):18996–9006. https://doi.org/10.1016/J.IJHYDENE.2012.09.139.

[48] Braaten JP, Ogawa S, Yarlagadda V, Kongkanand A, Litster S. Studying Pt-based fuel cell electrode degradation with nanoscale X-ray computed tomography. J. Power Sources Dec. 2020;478:229049. https://doi.org/10.1016/j.jpowsour.2020.229049.

[49] Khan ZA, Tranter T, Agnaou M, Elkamel A, Gostick J. Dual network extraction algorithm to investigate multiple transport processes in porous materials: image-based modeling of pore and grain scale processes. Comput. Chem. Eng. Apr. 2019; 123:64–77. https://doi.org/10.1016/j.compchemeng.2018.12.025.

[50] Khan ZA, Elkamel A, Gostick JT. Efficient extraction of pore networks from massive tomograms via geometric domain decomposition. Adv. Water Resour. Nov. 2020; 145:103734. https://doi.org/10.1016/j.advwatres.2020.103734.

[51] Silin D, Patzek T. Pore space morphology analysis using maximal inscribed spheres. Phys. A: Stat. Mech. Appl. 2006;371(2):336–60. https://doi.org/10.1016/j.physa.2006.04.048.

[52] Gostick J, et al. PoreSpy: A Python toolkit for quantitative analysis of porous media images. J. Open Source Softw. 2019;4(37):1296.
[53] Gostick J, et al. OpenPNM: a pore network modeling package. Comput. Sci. Eng. Jul. 2016;18(4):60–74. https://doi.org/10.1109/MCSE.2016.49.
[54] "New Insights into Perfluorinated Sulfonic-Acid Ionomers | Chemical Reviews." https://doi.org/10.1021/acs.chemrev.6b00159 (accessed Jun. 23, 2023).
[55] Bosanquet C. British TA report BR-507. September. 1944.
[56] Pollard WG, Present RD. On gaseous self-diffusion in long capillary tubes. Phys. Rev. Apr. 1948;73(7):762–74. https://doi.org/10.1103/PhysRev.73.762.
[57] Newman J, Thomas-Alyea KE. Electrochemical systems. John Wiley & Sons; 2012.
[58] Fuller EN, Schettler PD, Giddings JC. New method for prediction of binary gas-phase diffusion coefficients. Ind. Eng. Chem. 1966;58(5):18–27.
[59] Siddique NA, Liu F. Process based reconstruction and simulation of a three-dimensional fuel cell catalyst layer. Electrochim. Acta Jul. 2010;55(19):5357–66. https://doi.org/10.1016/J.ELECTACTA.2010.04.059.
[60] Subramanian NP, Greszler TA, Zhang J, Gu W, Makharia R. Pt-oxide coverage-dependent oxygen reduction reaction (ORR) kinetics. J. Electrochem. Soc. Mar. 2012;159(5):B531. https://doi.org/10.1149/2.088205jes.
[61] Neyerlin KC, Gu W, Jorne J, Gasteiger HA. Determination of catalyst unique parameters for the oxygen reduction reaction in a PEMFC. J. Electrochem. Soc. Aug. 2006;153(10):A1955. https://doi.org/10.1149/1.2266294.
[62] Borup RL, Kusoglu A, Weber AZ. "M2FCT: Million Mile Fuel Cell Truck Consortium," Los Alamos National Lab. (LANL), Los Alamos, NM (United States), LA-UR-21-32315. Accessed: Nov. 08, 2022. [Online]. Available: https://www.osti.gov/biblio/1836967; Dec. 2021.
[63] Cullen DA, et al. New roads and challenges for fuel cells in heavy-duty transportation. Nat. Energy May 2021;6(5):462–74. https://doi.org/10.1038/s41560-021-00775-z.
[64] Chen S, Gasteiger HA, Hayakawa K, Tada T, Shao-Horn Y. Platinum-alloy cathode catalyst degradation in proton exchange membrane fuel cells: nanometer-scale compositional and morphological changes. J. Electrochem. Soc. Nov. 2009;157(1):A82. https://doi.org/10.1149/1.3258275.
[65] Schneider P, et al. Impact of platinum loading and layer thickness on cathode catalyst degradation in PEM fuel cells. J. Electrochem. Soc. Feb. 2023;170(2):024506. https://doi.org/10.1149/1945-7111/acb8df.
[66] Sheng W, Gasteiger HA, Shao-Horn Y. Hydrogen oxidation and evolution reaction kinetics on platinum: acid vs alkaline electrolytes. J. Electrochem. Soc. 2010;157(11):B1529–36.
[67] Zhang J, Litteer BA, Gu W, Liu H, Gasteiger HA. Effect of hydrogen and oxygen partial pressure on Pt precipitation within the membrane of PEMFCs. J. Electrochem. Soc. Aug. 2007;154(10):B1006. https://doi.org/10.1149/1.2764240.
[68] Padgett E, et al. Mitigation of PEM fuel cell catalyst degradation with porous carbon supports. J. Electrochem. Soc. 2019;166(4):F198–207. https://doi.org/10.1149/2.0371904jes.
[69] Kim Y, et al. Fabrication of platinum group metal-free catalyst layer with enhanced mass transport characteristics via an electrospraying technique. Mater. Today Energy 2021;20:100641.
[70] Lange KJ, Sui P-C, Djilali N. Pore scale simulation of transport and electrochemical reactions in reconstructed PEMFC catalyst layers. J. Electrochem. Soc. Oct. 2010;157(10):B1434. https://doi.org/10.1149/1.3478207.
[71] Lange KJ, Sui P-C, Djilali N. Determination of effective transport properties in a PEMFC catalyst layer using different reconstruction algorithms. J. Power Sources Jun. 2012;208:354–65. https://doi.org/10.1016/J.JPOWSOUR.2011.11.001.
[72] Satjaritanun P, Cetinbas FC, Hirano S, Zenyuk IV, Ahluwalia RK, Shimpalee S. Hybrid lattice boltzmann agglomeration method for modeling transport phenomena in polymer electrolyte membrane fuel cells. J. Electrochem. Soc. Apr. 2021;168(4):044508. https://doi.org/10.1149/1945-7111/abf217.
[73] Sabharwal M, Secanell M. Understanding the effect of porosity and pore size distribution on low loading catalyst layers. Electrochim. Acta Jul. 2022;419:140410. https://doi.org/10.1016/j.electacta.2022.140410.
[74] Jinnouchi R, et al. The role of oxygen-permeable ionomer for polymer electrolyte fuel cells. Nat. Commun. Dec. 2021;12(1):4956. https://doi.org/10.1038/s41467-021-25301-3.